Constraints from GPS measurements on the dynamics of deformation in Anatolia and the Aegean

Philip England, Gregory Houseman, Jean-Mathieu Nocquet

AGU PUBLICATIONS

JGR

Journal of Geophysical Research: Solid Earth

RESEARCH ARTICLE
10.1002/2016JB013382

Special Section:
Stress at Active Plate Boundaries—Measurement and Analysis, and Implications for Seismic Hazard

Constraints from GPS measurements on the dynamics of deformation in Anatolia and the Aegean

Philip England[1], Gregory Houseman[2], and Jean-Mathieu Nocquet[3]

[1]Department of Earth Sciences, University of Oxford, Oxford, UK, [2]Institute of Geophysics and Tectonics, University of Leeds, Leeds, UK, [3]Observatoire de la Côte d'Azur, Université Côte d'Azur, IRD, CNRS, Valbonne, France

Abstract We estimate the strength of the lithosphere in Anatolia and the Aegean, and the boundary forces acting upon it, using a dynamical model that treats the lithosphere as a thin fluid sheet deforming in response to variations in gravitational potential energy. This model has one free material parameter, the power law exponent, *n*, of the vertically averaged rheology of the lithosphere, and two parameters that specify the forces per unit length applied to its edges. Solutions to this model that best fit the velocities of 346 reliable GPS sites require an effective viscosity of the lithosphere of 10^{22} to 10^{21} Pa s at strain rates of 10 to 100 nanostrain per year. The best-fitting force at the Arabia-Anatolia boundary is consistent with the lithostatic pressure due to the high topography there, and the force at the Nubia-Aegean boundary is consistent with the contrast in lithostatic pressure across that boundary. No additional force, from "slab rollback" or basal tractions due to convection in the mantle, is required to explain the observations. These results are supported by scaling relations derived from approximate analytical solutions. The inverse relationship between the viscosity of the lithosphere and deviatoric stress produces strong slowly deforming regions in the Southern Aegean and Central Anatolia whose motions resemble those of microplates. The distribution of geodetic strain rates within the region, and the partitioning between normal and strike-slip faulting, are explained by the interplay between boundary conditions, internal variations in gravitational potential energy, and the power law rheology of the lithosphere.

Key Points:
- Physical model that treats lithosphere of Anatolia and the Aegean as a fluid sheet fits GPS velocities with RMS misfit of 5 mm/yr
- Distributions of strain, earthquakes, and active faulting determined by lateral variations in gravitational potential energy of lithosphere
- Variation in strength of lithosphere not required to explain large-scale deformation though moderate weakening likely near N Anatolia fault

Supporting Information:
- Supporting Information S1
- Table S1

Correspondence to:
P. England,
philip@earth.ox.ac.uk

Citation:
England, P., G. Houseman, and J.-M. Nocquet (2016), Constraints from GPS measurements on the dynamics of deformation in Anatolia and the Aegean, *J. Geophys. Res. Solid Earth*, *121*, 8888–8916, doi:10.1002/2016JB013382.

Received 25 JUL 2016
Accepted 9 NOV 2016
Accepted article online 15 NOV 2016
Published online 3 DEC 2016

1. Introduction

We investigate the forces responsible for the deformation of Anatolia and the Aegean, the continental region that lies between eastern Turkey and the coasts of the Eastern Mediterranean and Ionian Seas (Figure 1). The region is bounded to the south by the Nubian and Arabian plates and to the north by stable Eurasia. Hereinafter, we use the term Eurasia to refer to the part of the Eurasian continent and its surrounding ocean floor that exhibits negligible internal deformation and, unless otherwise specified, velocities are relative to Eurasia. Nubia and Arabia move roughly northward whereas Anatolia moves northwest-to-westward, and western Turkey and Greece move west-to-southwestward (Figure 2a) [*Aktuğ et al.*, 2009; *Floyd et al.*, 2010; *McClusky et al.*, 2000; *Reilinger et al.*, 2006]. Kinematic descriptions of the motion of Anatolia and the Aegean have labeled it as "extrusion" or "escape" [e.g., *Armijo et al.*, 1999, 2003; *Şengör et al.*, 1985] or have ascribed it to the "rollback" of the Nubian slab beneath the southern Aegean [e.g., *Le Pichon*, 1982; *Le Pichon and Kreemer*, 2010; *Royden*, 1993]. Dynamical explanations for this motion attribute it to differences in gravitational potential energy between eastern Turkey and the southern Aegean (Figure 3), or to tractions applied to the base of the lithosphere by flow of the mantle [e.g., *Faccenna et al.*, 2014; *Le Pichon*, 1982; *Le Pichon and Angelier*, 1979; *Le Pichon and Kreemer*, 2010; *McKenzie*, 1972, 1978].

Although the large-scale motions of Anatolia and the Aegean relative to Eurasia can be described approximately by a rigid-body rotation with a pole near the Nile delta [*Le Pichon and Kreemer*, 2010; *Reilinger et al.*, 2006], active faults pervade the region and GPS velocities increase systematically by 20 mm/yr from east to west [e.g., *Aktuğ et al.*, 2009, 2013; *Floyd et al.*, 2010; *Goldsworthy and Jackson*, 2000, 2001; *Goldsworthy et al.*, 2002; *Jackson*, 1994; *Jackson and McKenzie*, 1988; *Reilinger et al.*, 2006; *Şaroglu et al.*, 1992; *Shaw and Jackson*, 2010; *Taymaz et al.*, 1991a] (see Figures 1, 2, and 4b). This deformation results in widespread large shallow earthquakes (Figure 1b) whose focal mechanisms vary from thrust and reverse faulting along the western and southern margins of the region to normal faulting throughout mainland Greece and western Turkey, to normal-plus-strike-slip faulting in the northern Aegean, and to strike-slip faulting on the north and southeastern margins of Anatolia.

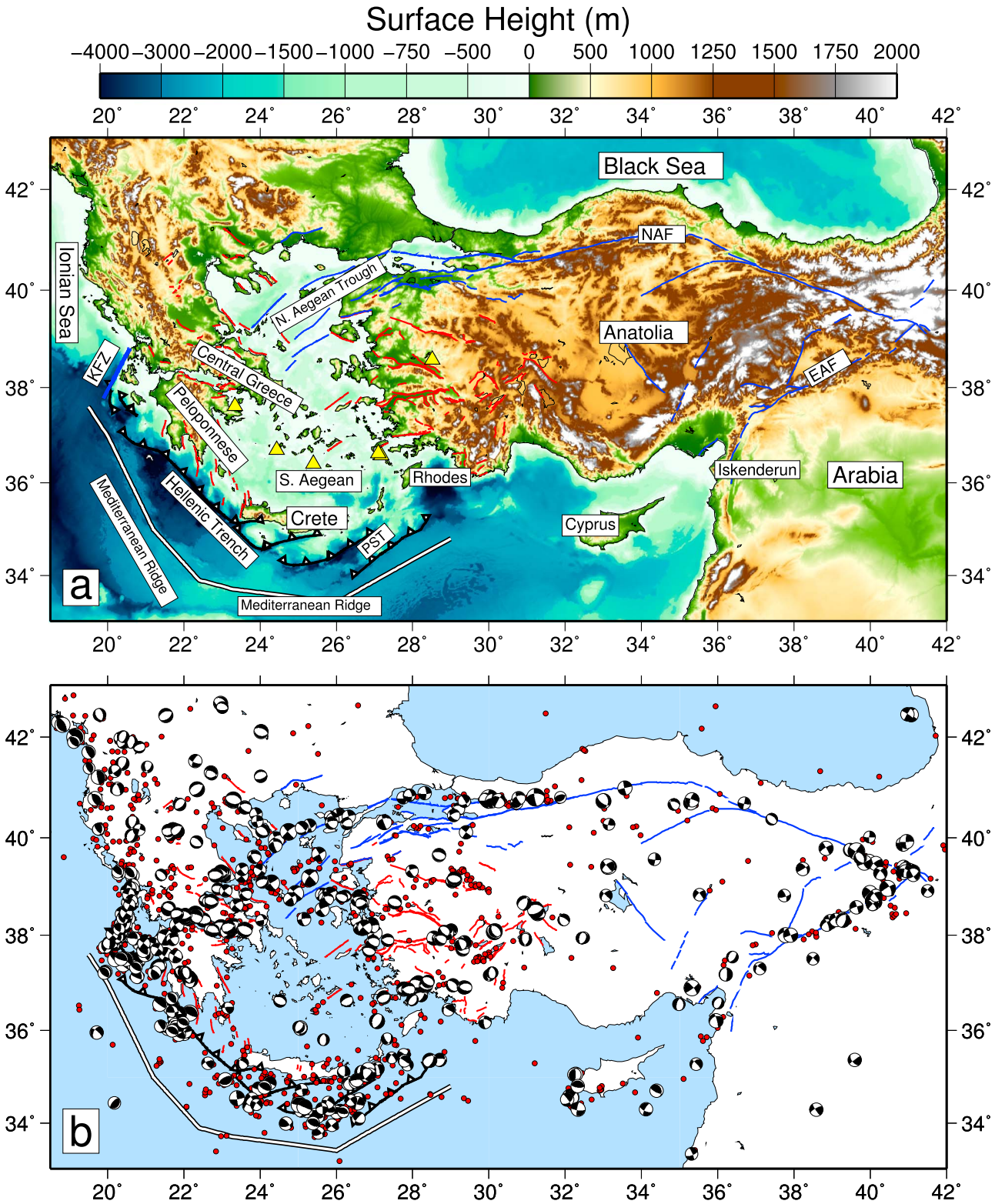

Figure 1. Tectonic setting. (a) Location map showing places referred to in the text. KFZ: Kefalonia Fault Zone; PST: Pliny and Strabo Trenches; NAF: North Anatolian Fault; EAF: East Anatolian Fault. Active faults of the region are shown in blue (strike slip) or red (normal) [*Goldsworthy and Jackson*, 2000, 2001; *Goldsworthy et al.*, 2002; *Şaroglu et al.*, 1992]. Yellow triangles indicate the locations of the active volcanoes of the Aegean arc. (b) Seismic activity of the region. Dots show the epicenters of earthquakes between 1960 and 2007 with hypocenters shallower than 33 km [*International Seismological Centre*, 2011]. Focal mechanisms from the GCMT catalog [*Dziewonski et al.*, 1981; *Ekström et al.*, 2012] and from *Jackson and McKenzie* [1988]; *Shaw and Jackson* [2010].

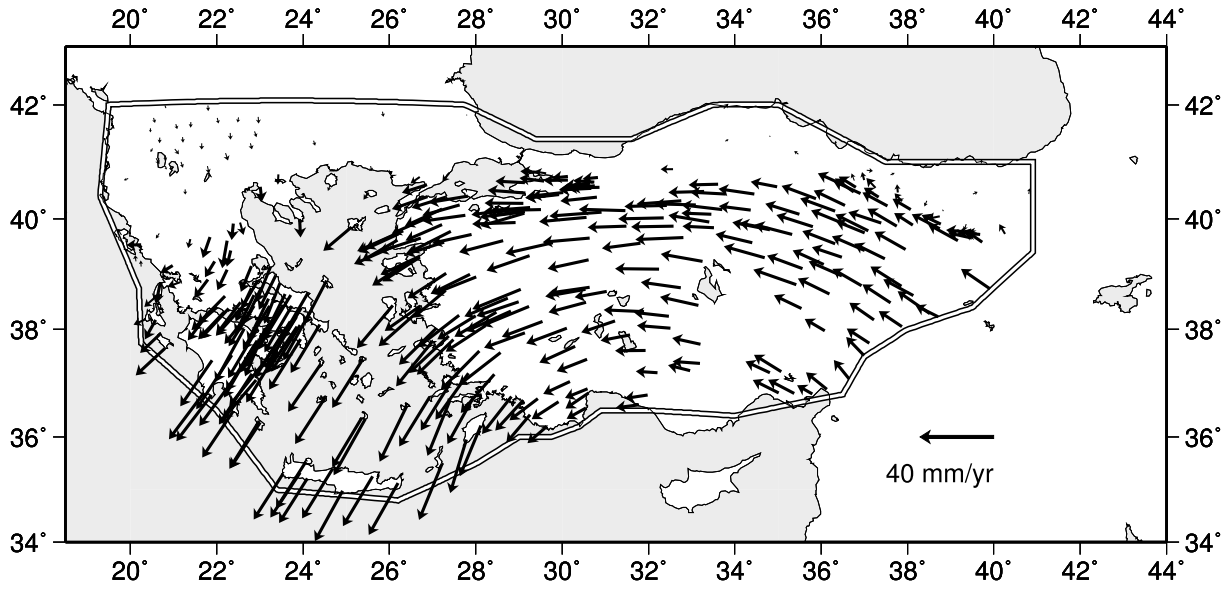

Figure 2. Velocities, relative to Eurasia, of the 346 GPS sites in the Aegean and Anatolia used as constraints on the physical model (section 2). Double line shows region in which the calculations of this paper are carried out (Figure 3).

The velocity differences of ~20 mm/yr within Anatolia and the Aegean have been described by kinematic models that contain between two and six elastic blocks, with permanent deformation being concentrated around their edges [e.g., *Le Pichon et al.*, 1995; *McClusky et al.*, 2000; *Nyst and Thatcher*, 2004; *Reilinger et al.*, 2006]. Alternatively, they have been interpreted as the strain of a ductile lithosphere within which stronger enclaves are embedded [e.g., *Billiris et al.*, 1991; *Clarke et al.*, 1998; *Davies et al.*, 1997; *Hollenstein et al.*, 2008] that deforms in response to boundary tractions and internal gradients in gravitational potential energy [e.g., *Hatzfeld et al.*, 1997; *Le Pichon*, 1982; *Le Pichon and Angelier*, 1979; *Le Pichon and Kreemer*, 2010; *Martinod et al.*, 2000; *McKenzie*, 1972, 1978; *Özeren and Holt*, 2010].

The differences among these descriptions of the motions of Anatolia and the Aegean, and of their internal deformation, are rooted in questions about the relative magnitudes of forces acting on the lithosphere, and about the importance of lateral variations in its strength. We investigate these issues using a physical model constrained by a regional-scale GPS velocity field. First, we show that the stresses associated with lateral differences in gravitational potential energy are large enough to cause the observed deformation of the lithosphere. Second, we show that the distribution of this deformation does not require strong lateral variations in the intrinsic physical properties of the lithosphere. Furthermore, we show that the boundary tractions required to explain the observed field of deformation are consistent with the gravitational potential energy (GPE) contrasts across the Aegean and Anatolian boundaries and that tractions acting on the base of the lithosphere are not required to explain the deformation.

2. GPS Observations

Our analysis is constrained by measurements of crustal velocities made using the Global Positioning System (GPS). *Nocquet* [2012] combined 24 GPS studies in a common reference frame, checking for consistency among solutions and reevaluating uncertainties in velocity. We added measurements by *Aktuğ et al.* [2013, 2015], *Ozener et al.* [2010]; *Tatar et al.* [2012], and *Yavaşoğlu et al.* [2010] as individual solutions and made a full combination using the procedures of *Nocquet* [2012]. We then selected, using information from the original publications, only those stations that were occupied on at least three occasions, over a time span of longer than 4 years. All sites having a formal error greater than 2 mm/yr in their velocity were eliminated, leaving 346 measurements of horizontal velocity within the region shown in Figure 2. These are considerably fewer than the 872 velocities used by *Özeren and Holt* [2010], but that data set contained many sites reported by two or more publications, and many sites that we have excluded by the criteria of number and duration of occupations. We therefore expect that the data set we use, in addition to having more information in Anatolia [*Aktuğ et al.*, 2013, 2015; *Ozener et al.*, 2010; *Tatar et al.*, 2012; *Yavaşoğlu et al.*, 2010], is appreciably less

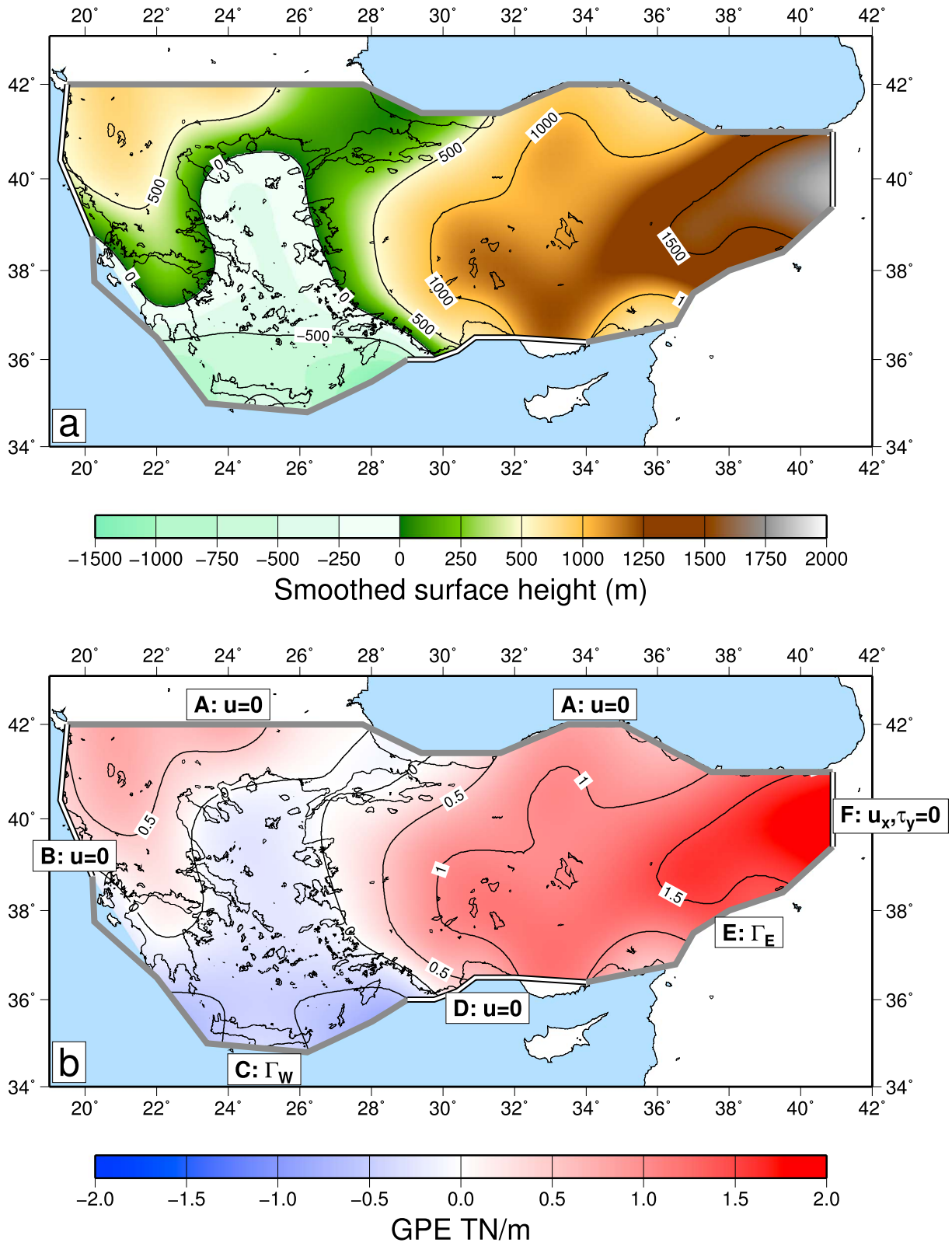

Figure 3. Topography and GPE within the calculation domain (delineated by labeled boundary segments). (a) Surface height within the calculation domain smoothed with a Gaussian filter of width 100 km. (b) GPE calculated from surface height (section 3.1, equation (5), and parameters given in Table 1). Lines labeled A to F indicate the locations at which different boundary conditions are applied in the calculations. Conditions of zero velocity are applied on segments A, B, and D. Forces per unit length Γ_W and Γ_E are applied to segments C and E, as discussed in the text (section 3.2). Zero tangential traction and zero normal velocity are applied to the north-south boundary segment F.

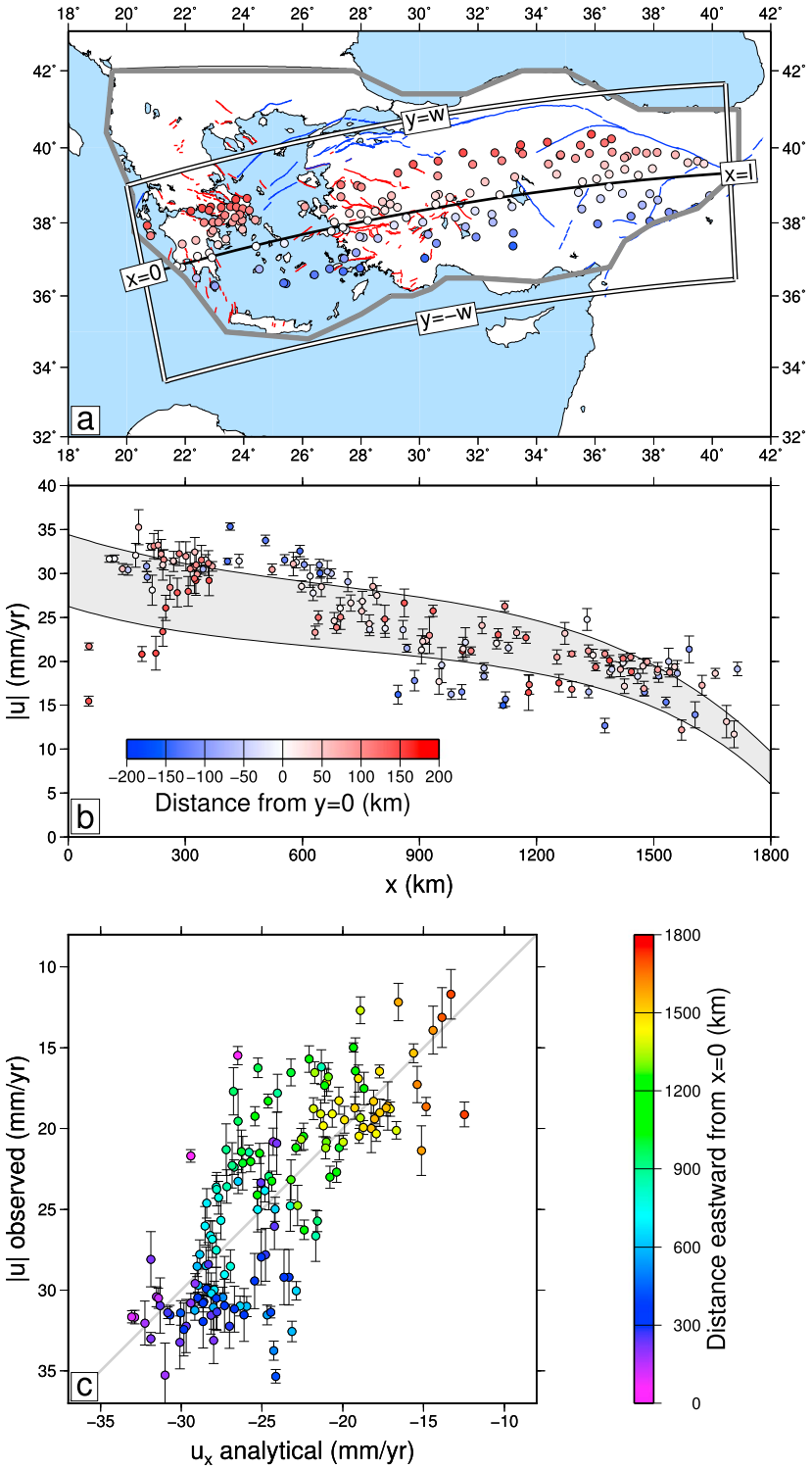

Figure 4. Illustration of analytical solution for the velocity in a rectangular thin viscous sheet (Appendix A). (a) The geographical region of interest (bounded by gray lines) is approximated by a box of east-west length *l* and north-south dimension 2*w* (double lines); the slight curvature is neglected. Dots show locations of GPS sites whose velocities (magnitudes) are plotted in Figure 4b); sites within 150 km of the profile are used, except those on the Eurasian or Arabian plates. (b) Projection of magnitudes of GPS velocities along the line $x = 0$. Gray-shaded region shows the range of velocities calculated for the best-fitting analytical solution (equation (A6), and see section 4.) Upper boundary of gray shade corresponds to the solution at $y = 0$, lower bound to the solution at $y = \pm 150$ km. (c) Comparison between analytical solution and observations (in the analytical solution positive u_x is eastward).

influenced by measurement error. The mean spacing between sites is about 50 km, though sites within the Aegean Sea are separated by up to 100 km.

3. Physical Model

3.1. Mathematical Formulation

We treat the continental lithosphere as a sheet of fluid whose deformation is determined by the vertical averages of its physical properties and of the forces acting upon it—the thin sheet approximation [*Bird and Piper*, 1980; *England and McKenzie*, 1983; *Houseman and England*, 1986] (see *Schmalholz et al.* [2014], for a recent discussion that corrects some misapprehensions that have arisen in the literature concerning this approximation). Geodetic measurements of the deformation of the lithosphere are taken at the top of the upper crust, which in general deforms elastically. We take the view that, except during the postseismic intervals of nearby earthquakes, the strain of this thin elastic layer follows closely the ductile strain of the layer beneath [e.g., *Bird and Piper*, 1980; *Bourne et al.*, 1998; *Houseman and England*, 1986]. This view contrasts with interpretations of velocity fields that treat the lithosphere as an elastic medium whose surface deformation is controlled by the slip of dislocations buried within it [e.g., *Hammond et al.*, 2011; *Meade et al.*, 2002; *Meade and Hager*, 2005; *Reilinger et al.*, 2006; *Wallace et al.*, 2007].

Garthwaite and Houseman [2011] compared 3-D calculations with the results of the 2-D thin-sheet model and showed that in the absence of strong vertical stratification of physical properties, differences are minor, provided that the horizontal scale of the deforming zone and the length scale over which significant changes in boundary condition occur, are greater than the thickness of the lithosphere. The first of these conditions is met: the horizontal scales of the region of interest are of the order of a thousand kilometers whereas the lithospheric thickness is of the order of a hundred kilometers. The second condition may be violated in small regions, such as either end of the Hellenic plate boundary, where there are abrupt changes in boundary condition.

The depth-averaged rheology of the thin sheet is described by a power law relation between deviatoric stress and strain rate:

$$\overline{\tau}_{ij} = B\dot{E}^{\left(\frac{1}{n}-1\right)}\dot{\varepsilon}_{ij} \tag{1}$$

where $\dot{\varepsilon}_{ij}$ is the ijth component of the strain rate tensor, assumed constant with depth through the sheet, $\overline{\tau}_{ij}$ is the ijth component of the deviatoric stress, with the overbar denoting averages over the thickness, L, of the lithosphere, n is the power law exponent for the rheology, and

$$\dot{E} = \left(\dot{\varepsilon}_{kl}\dot{\varepsilon}_{kl}\right)^{\frac{1}{2}} \tag{2}$$

is the second invariant of the strain rate tensor and the convention of summation over repeated indices applies. The fluid is assumed to be incompressible ($\dot{\varepsilon}_{kk} = 0$).

Sonder and England [1986] showed that equation (1) closely approximates the vertically averaged rheology of a lithosphere deforming by a combination of creep mechanisms, which are largely temperature-dependent, and frictional mechanisms, which depend principally on pressure. Furthermore, if the brittle upper crust is cut by numerous faults, then it may be appropriate to describe its long-term deformation field by a power law rheology of the form of equation (1) [e.g., *Nanjo and Turcotte*, 2005]. The single parameter, n, allows the depth-averaged rheology for the lithosphere to range from Newtonian behavior (when $n = 1$) to almost plastic behavior for large n.

The quantity

$$\eta_{\text{eff}} = \frac{1}{2}B\dot{E}^{\left(\frac{1}{n}-1\right)} = \frac{1}{2}B^{n}\overline{T}^{(1-n)}, \tag{3}$$

where $\overline{T}$ is the second invariant of the vertically averaged deviatoric stress tensor, $\left(\overline{\tau}_{kl}\overline{\tau}_{kl}\right)^{\frac{1}{2}}$, is commonly referred to as the effective viscosity, by analogy with the viscosity of a Newtonian fluid in the case that $n = 1$. Note that for $n \neq 1$ the effective viscosity depends on the deviatoric stress, or equivalently upon strain rate, so that lithosphere of spatially invariant viscosity coefficient, B, will in general exhibit lateral variation in its effective viscosity.

Table 1. Notation

Parameter	Definition	Value/Reference
B	Viscosity coefficient	equation (1)
g	Acceleration due to gravity	9.8 m s^{-2}
h	Surface height	Figures 1 and 3
h_0	Reference surface height	100 m
L	Thickness of the lithosphere	100 km
S	Crustal thickness	
S_0	Reference crustal thickness	35 km
u_i	ith component of velocity	
U_0	velocity scale	equation (8)
$\dot{\varepsilon}_{ij}$	ijth component of strain rate	
$\dot{E}$	Second invariant of strain rate tensor	equation (2)
η_{eff}	Effective viscosity	equation (3)
Γ	Gravitational potential energy per unit surface area	N m^{-1} or J m^{-2}
ρ_c	Density of crust	2800 kg m^{-3}
ρ_m	Density of mantle	3200 kg m^{-3}
τ_{ij}	ijth component of deviatoric stress	

The equations governing the deformation of the thin sheet (equation (A14)) express the balance between horizontal gradients of the deviatoric stress required to deform the sheet and gradients in its gravitational potential energy per unit area (GPE). We estimate the GPE of lithospheric columns using the distribution of surface height shown in Figure 3a, having applied a Gaussian filter of width 100 km to the surface height within the calculation domain. We define a reference column of lithosphere, with crustal thickness S_0, surface height h_0, and densities as stated in Table 1. Surface height above sea level, h, is related to crustal thickness, S, under the assumption of Airy isostatic balance

$$S - S_0 = \frac{\rho_m}{\rho_m - \rho_c}\left(h - h_0\right), \tag{4}$$

where ρ_c and ρ_m are the average densities of crust and mantle. For uniform crust overlying uniform mantle, the difference in GPE between the reference column, of GPE Γ_0, and a column with crust of thickness S is

$$\Gamma - \Gamma_0 = g\rho_c\left(h - h_0\right)\left(S_0 + \frac{\rho_m\left(h - h_0\right)}{2\left(\rho_m - \rho_c\right)}\right) \tag{5}$$

where g is the acceleration due to gravity; for columns with $h < 0$ these expressions are adjusted for the contribution from the water column [*Haxby and Turcotte*, 1978].

Within the continental lithosphere of the region the GPE $(\Gamma - \Gamma_0)$ varies from a high of 2 TN m^{-1} in the east to a low of −1 TN m^{-1} in the southernmost Aegean (Figure 3b). The assumption of Airy isostasy is not critical; if isostatic compensation is maintained in part by density variations in the mantle, then the GPE for a given surface height would be slightly higher or lower than that given by equation (5), resulting in minor local adjustments to the velocity field. The small size of isostatic gravity anomalies in the region [*Balmino et al.*, 2012] rules out significant nonisostatic contribution to GPE from lifting of the lithosphere by convective tractions applied to its base, sometimes referred to as "dynamic topography" [e.g., *Molnar et al.*, 2015, Figure 5].

3.2. Calculation Domain and Boundary Conditions

We divide the border to the calculation domain into six sections whose lengths and locations are dictated by their geological setting (Figure 3b). The adoption of a small number of long boundary segments is justified by a fundamental aspect of the governing equations: a condition of stress or velocity, when applied over a length w of boundary, influences strain rates over a distance from that boundary that is $\sim w/(\alpha\sqrt{n})$, where n is the exponent in the power law rheology (equation (1)) and α depends on the nature of the boundary condition [*England et al.*, 1985; *Sonder et al.*, 1986]. When the boundary condition is one of normal velocity or traction,

$\alpha \sim 1$; when the condition is tangential, the length scale is 4 times shorter ($\alpha \sim 4$). It follows that any variation in boundary condition over a scale that is small compared with the size of the region of interest has only a local influence and does not significantly affect the distribution of stresses and velocities far from that boundary. This assertion is supported by investigation of alternative, more complex, boundary conditions in section 5.4.

The reference frame is fixed to Eurasia and we set velocity to zero along a boundary (segment A in Figure 3b) that follows the southern edge of the Black Sea, which we presume, from the lack of deformation within and to the north of it, to be part of Eurasia. At its western end, segment A runs to the north of the regions of extension and convergence in Greece. Although there is some active deformation to the north of this line, velocities there are generally lower than 2–3 mm/yr relative to Eurasia [*Burchfiel et al.*, 2006; *Kotzev et al.*, 2006].

We place the boundary between the Aegean lithosphere and the Nubian plate along a line running to the landward side of the Hellenic, Pliny, and Strabo Trenches, which represent the outcrops of major faults at the southern border of the Aegean [e.g., *Le Pichon and Angelier*, 1979; *Mascle and Chaumillon*, 1998]. Segment C in Figure 3b corresponds approximately to the downdip limit of shallowly dipping thrust-faulting earthquakes on the plate interface and represents the boundary between the accretionary prism and the overriding Aegean continental crust [e.g., *Shaw and Jackson*, 2010]. It is probable that 80% to 90% of the convergence across this boundary occurs by steady aseismic slip on the subduction interface [*Jackson and McKenzie*, 1988; *Reilinger et al.*, 2009; *Vernant et al.*, 2014] (though see *Ganas and Parsons* [2009] for an alternative viewpoint); it is therefore difficult to constrain the velocity condition for this boundary. Instead, we apply a normal force per unit length, Γ_W, and allow this to be a free parameter in the calculations.

Similarly, it is appropriate to specify a normal force per unit length at the boundary between Arabia and Anatolia (segment E in Figure 3b); again we allow this force, Γ_E, to be a free parameter in the calculations. We continue the calculation domain to 41°E (segment F in Figure 3b) for simplicity setting the east-west velocity and the tangential traction on this boundary to be zero. This segment is short enough that its location and conditions do not appreciably influence velocities throughout most of the calculation domain.

The relative velocities across the boundaries between Turkey and Nubia (segment D in Figure 3b) and between the Ionian Sea and the northwestern part of the region (segment B) are poorly constrained. Segment D lies along a diffuse zone of deformation between Rhodes and the Gulf of Iskenderun [e.g., *Aksu et al.*, 2009; *Hall et al.*, 2009; *ten Veen et al.*, 2004; *Woodside et al.*, 2002], and it is unclear what fraction of the relative motion between Nubia and Anatolia is absorbed south of the coast of Turkey. Equally, the rate of convergence across the boundary with the Ionian Sea is a few millimeters a year [e.g., *D'Agostino et al.*, 2008] and it is unclear what fraction of that rate is absorbed offshore. In order to maintain the simplicity of our calculations we initially set the velocity on each segment to zero, investigating more complex boundary conditions later (section 5.4).

4. Preliminary Analysis

We first investigate the observed distribution of velocities using an analytical solution for the flow of a thin sheet of Newtonian fluid (equation (A6) in section A1). In this approximation, the geometrically complex boundary conditions on Anatolia and the Aegean are replaced by a box bounded by planes at $x = 0$, l, and at $y = \pm w$ (Figure 4a). The planes at $y = \pm w$ represent the northern and southern boundaries of Anatolia and the Aegean. The plane $x = 0$ approximates the Hellenic plate boundary, and $x = l$ approximates the eastern boundary to Anatolia. The GPE in this box varies linearly from Γ_W at $x = 0$ to Γ_E at $x = l$, giving a gradient of GPE that is

$$\frac{\Gamma_E - \Gamma_W}{l} = \frac{\Delta\Gamma}{l}. \tag{6}$$

The plane $y = w$ is taken to have zero velocity, i.e., to be fixed to Eurasia. The plane $y = -w$ runs close to segments E, D, and part of C (Figure 3b). As discussed in section 3.2, the set of conditions along this boundary cannot be captured by a single parameter; to maintain the simplicity of the approximation, the velocity on this boundary is also set to zero. The boundary conditions on $x = 0, l$ are expressed as forces per unit length, $\Delta\Gamma_W$, $\Delta\Gamma_E$, which represent contrasts in GPE across the boundaries (positive values of these quantities correspond to lower GPE outside the boundary, therefore, to a net extensional force acting on that boundary: equations (A4) and (A5)).

The east-west dimension, l, of the geographical region of interest is about 1800 km (from 20°E to 41°E, Figure 4a). The north-south dimension varies from about 400 km in the east to 800 km in the west (Figure 4a); we adopt a value of 600 km for the width of the box ($w = 300$ km). We do not expect the approximate solution to hold near the coastlines of Turkey, where the configuration of the boundaries is complex. In Figure 4b we compare this solution with the variation in GPS velocities along a swath from eastern Anatolia to the Hellenic plate boundary that is 300 km wide.

The analytical solution (equation (A6)) has three velocity scales: $\Delta\Gamma w^2/(2\eta L l)$ and ($\Delta\Gamma_W$ or $\Delta\Gamma_E$) $\times 4w/(\pi^2\eta L)$, where η is the viscosity of the lithosphere and L its thickness. We found, by linear least squares inversion, the values of these parameters for which the analytical solution best fits the observations. The best-fit velocity scale associated with the GPE difference, $\Delta\Gamma$, is −29 mm/yr. With $\Delta\Gamma \sim 3 \times 10^{12}$ N m^{-1} (Figure 3b), $l \sim 1800$ km, $w \sim 300$ km, and $L \sim 100$ km, this scale yields an estimate of $\sim 10^{21}$ Pa s for the viscosity of the lithosphere. The best-fitting velocity scales associated with the GPE difference at $x = 0$ and l, $\Delta\Gamma_W$, and $\Delta\Gamma_E$ are, respectively, 7 mm/yr and 22 mm/yr; with $\eta \sim 10^{21}$ Pa s, these scales give forces per unit length of $\Delta\Gamma_W \sim 0.2$ TN m^{-1} on $x = 0$ and $\Delta\Gamma_E \sim 0.6$ TN m^{-1} (both in relative tension) on $x = l$.

The approximate solution (Figures 4b and 4c) displays the principal features of the variation in velocity between eastern Anatolia, despite the considerable differences between the idealized distribution of GPE (equation (6)) and that shown in Figure 3b. This analysis provides evidence that the large-scale deformation of the region is described by the balance between gradients of GPE and deviatoric stress in the lithosphere.

5. Numerical Experiments

5.1. Means of Solution

We solve the governing equations (equation (A14)) subject to the boundary conditions described in section 3.2, and with the distribution of GPE derived from topography (section 3.1, Figure 3b), using a finite element approximation to the equations for deformation on the surface of a sphere (see section A2). The finite element mesh contains 5400 nodal points, 346 of which are placed at the locations of the GPS sites. The mean spacing between nodal points is approximately 15 km, smaller than the typical spacings between GPS sites (Figure 2b). We checked the resolution of the calculations using meshes of 13,000 points and found that the RMS misfit to the observations differed by less than 1% between the two meshes.

As discussed in section A2, the equations are reduced to nondimensional forms that depend on a single parameter, the Argand number

$$Ar = \frac{g\rho_c L(1-\rho_c/\rho_m)}{B\left(U_0/L\right)^{1/n}}, \tag{7}$$

whose numerator represents a stress scale associated with density variations within the lithosphere and whose denominator represents the stress required to deform the lithosphere at a reference strain rate U_0/L (see equation (1)) [*England and McKenzie*, 1982].

In each calculation we chose a value for Ar which ensured that the maximum dimensionless velocity was of the order 1 and determined U_0 by minimizing the misfit function

$$M = \left[\frac{1}{N}\sum_{i=1}^{N}\left|\mathbf{u}_i^{\mathrm{GPS}} - U_0\mathbf{u}_i'\right|^2\right]^{\frac{1}{2}} \tag{8}$$

where $\mathbf{u}_i^{\mathrm{GPS}}$ is the velocity of the ith GPS site, $\mathbf{u}_i'$ is the dimensionless velocity of the same site in the calculation, and N is the number of GPS sites. This value of U_0 then implies a value of the viscosity coefficient

$$B = \frac{g\rho_c L(1-\rho_c/\rho_m)}{Ar\left(U_0/L\right)^{1/n}}. \tag{9}$$

For any given calculation, the value of B is independent of the chosen value of Ar (see section A2). With the configuration of boundary conditions fixed, and with the distribution of GPE specified from the topography (Figure 3b), there are therefore only three free parameters: the exponent n in the power law rheology (equation (1)) and the magnitudes of Γ_W and Γ_E, the forces per unit length applied at the western and eastern boundaries (Figure 3b).

Table 2. Values of Parameters for the Best Fits (Figure 5) to the Observed Velocities (Figure 2), With n and the Boundary Forces Γ_W and Γ_E as Free Parameters[a]

	Γ_W TN m^{-1}	Γ_E TN m^{-1}	B Pa s$^{1/n}$	M (equation (8)) mm yr^{-1}
$n = 1$	0.625	−1.5	2.4×10^{21}	5.1
$n = 3$	1.0	−1.75	6.0×10^{11}	4.7
$n = 5$	1.25	−2.0	8.1×10^{9}	4.7
$n = 9$	1.625	−2.25	5.7×10^{8}	4.8

[a]For a Newtonian fluid, the viscosity, η, is equal to half the viscosity coefficient, B (equation (3)).

5.2. Estimation of Boundary Forces and Lithospheric Rheology

We calculated velocity fields varying Γ_W and $-\Gamma_E$ between zero and 10 TN m^{-1} in steps of 0.125 TN m^{-1}, and with $n = 1$, 3, 5, and 9. Solutions for $n = 5$ exhibit no feature that cannot be illustrated by the solutions for $n = 3$ and 9 so they are not shown, but the best-fitting parameters are listed in Table 2.

The misfits define an elongate valley on the $\Gamma_W - \Gamma_E$ plane (Figure 5) with minima near $\Gamma_E = -(\Gamma_W + 1$ TN m$^{-1})$. Values of Γ_W yielding the best fits to observations lie in the range 0.75 to 2 TN m^{-1} and those for Γ_E lie in

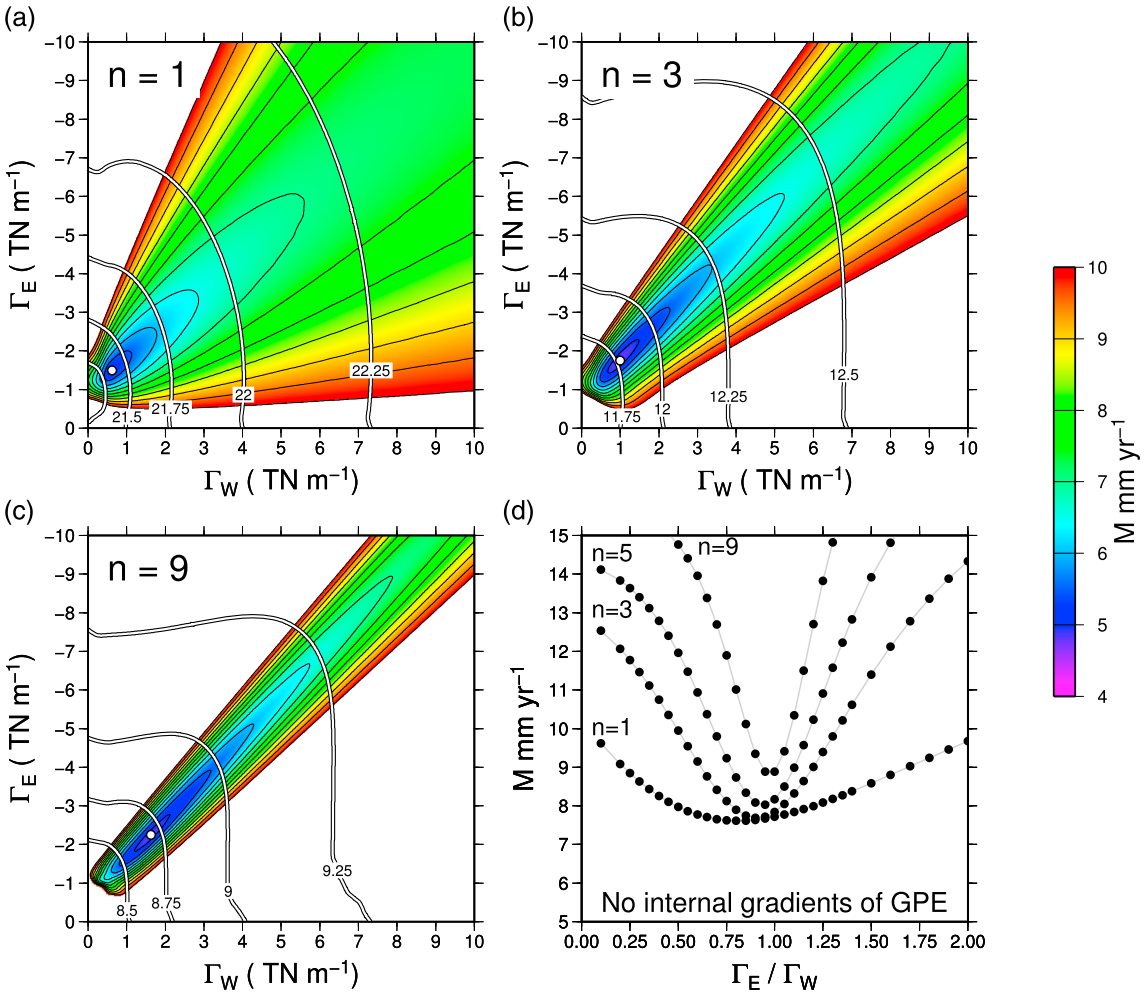

Figure 5. Root-mean-square misfits between calculated and observed velocity fields for a thin viscous sheet with (a) $n = 1$, (b) 3, and (c) 9 subjected to the boundary conditions and the internal distribution of gravitational potential energy shown in Figure 3b. Colors and black contours show the variation of RMS misfits (equation (8)) with Γ_W and Γ_E. Best-fitting combinations of Γ_W and Γ_E are shown by white dots (see Table 2). Double lines show contours of the logarithm to base 10 of the viscosity coefficient, B, for the solutions (units of Pa s$^{1/n}$). (d) Distributions of misfits for the case in which there are no internal gradients of GPE.

the range −1.5 to −2.25 TN m^{-1}. Because velocity gradients near the boundaries scale with the magnitude of the relevant boundary forces (Γ_E or Γ_W) raised to the power n (equation (1); see also equation (A12) in section A1.0.2), solutions that depart from the best-fitting valleys disagree sharply with the observations. This sensitivity causes the valleys in Figure 5 to become narrower as n increases.

Figure 5d shows the misfits for calculations in which the boundary conditions are varied, as above, but the GPE within the sheet is zero; this problem has only two free parameters, Γ_E / Γ_W and n. RMS misfits to the observations for these calculations are at least 50% greater than those in the case where internal variations in GPE are included ($M > 7.5$ mm/yr).

Figure 5 also displays contours of the viscosity coefficient B (equation (3)) that is implied by the velocity scale for each combination of Γ_E and Γ_W (see equation (8)). The Appendix A shows that the flow may be approximated by that of a power law fluid confined between two parallel plates and subjected to a constant pressure gradient representing the variation in GPE from west and east across the region. This approximation leads to a scaling relationship between the viscosity coefficient of the lithosphere and the differences in velocities and GPE across the region. From equation (A13), Appendix A

$$B \sim \frac{\Delta\Gamma w}{lL} \left[\frac{\sqrt{2}^{(n+1)}\, w}{u_{max}\,(n+1)} \right]^{1/n}. \tag{10}$$

With $u_{max} \sim 30$ mm/yr and the other variables as discussed in section 4, this scaling gives $B \sim 2\times10^{21}$, 3×10^{11}, 4×10^{9}, and 2×10^{8} Pa s$^{1/n}$ for $n = 1, 3, 5$, and 9, respectively. The corresponding values of B for the best-fitting solutions to the full thin-sheet equations (Table 2) are 2×10^{21}, 6×10^{11}, 8×10^{9} and 6×10^{8} Pa s$^{1/n}$; inspection of the contours of B in Figures 5a–5c shows that solutions with values of B obtained from equation (10) have misfits similar to the best-fitting solutions. The agreement between the scaling relationship and numerical solutions provides further support to the argument that the dynamics of Anatolia and the Aegean reflects the balance between gravitational potential energy and the stress required to deform the lithosphere.

5.3. Comparison With Observed Velocities

Figure 6 compares the observed velocities (Figure 2a) with those of the best-fitting thin-sheet calculations for $n = 3$ and $n = 9$. The variation by ∼90° in the orientations of velocity between eastern Anatolia and the southern Aegean, and the corresponding increase in velocity from ∼15 to ∼35 mm/yr relative to Eurasia, are reproduced by these calculations. The RMS misfit of the calculations to the observations (M, equation (8)) is less than 5 mm/yr while the RMS magnitude of the observed velocities (Figure 2a) is 20 mm/yr. Thus, a model with a single adjustable material parameter, n, the power law exponent in the rheology of the lithosphere, and two parameters that specify the forces per unit length (or, equivalently, the GPE) at the eastern and western boundaries can account for >90% of the variance in the velocity field.

The RMS misfits to the observations vary by less than 0.1 mm/yr between the best-fitting solutions for $n = 3$, 5, and 9 (Table 2). This result is at first sight surprising, because strain rates in power law fluids depend on deviatoric stress to the power n (equation (1)). As discussed in section 5.2, however, the flow is analogous to that of a channel of power law fluid whose velocity has the form $U_0\left(1 - |y/w|^{n+1}\right)$ (equation (A12)), where y is the distance from the center line of the channel. For a given value of U_0, solutions with different values of n differ appreciably only within narrow shear zones adjacent to the walls of the channel.

5.4. Additional Complexity in Boundary Conditions

Despite the broad agreement between observed and calculated velocity fields, systematic misfits remain at the level of 5–10 mm/yr, in particular, in the regions near Kefalonia (marked by K in Figures 6b and 6c), near Rhodes (R), in southeast Turkey (E), and near the North Anatolian fault (N). The misfits near Rhodes and Kefalonia resemble those that would be expected from the arguments in section 3.2, if the extensional normal traction were too low (R) or too high (K). Similarly, the misfits in southeast Turkey resemble those that would be expected if there were a tangential component of traction missing from the boundary conditions there, and the zone of dextral shear near the North Anatolian Fault is broader in the calculations than in the observations. Clearly, these minor misfits could be reduced if tractions were allowed to vary along the boundary segments and to include tangential components.

As discussed in section 3.2, the influence of an individual boundary segment extends no further into the sheet than the length of that segment [*England et al.*, 1985]. Subdivision of the boundary into many small segments

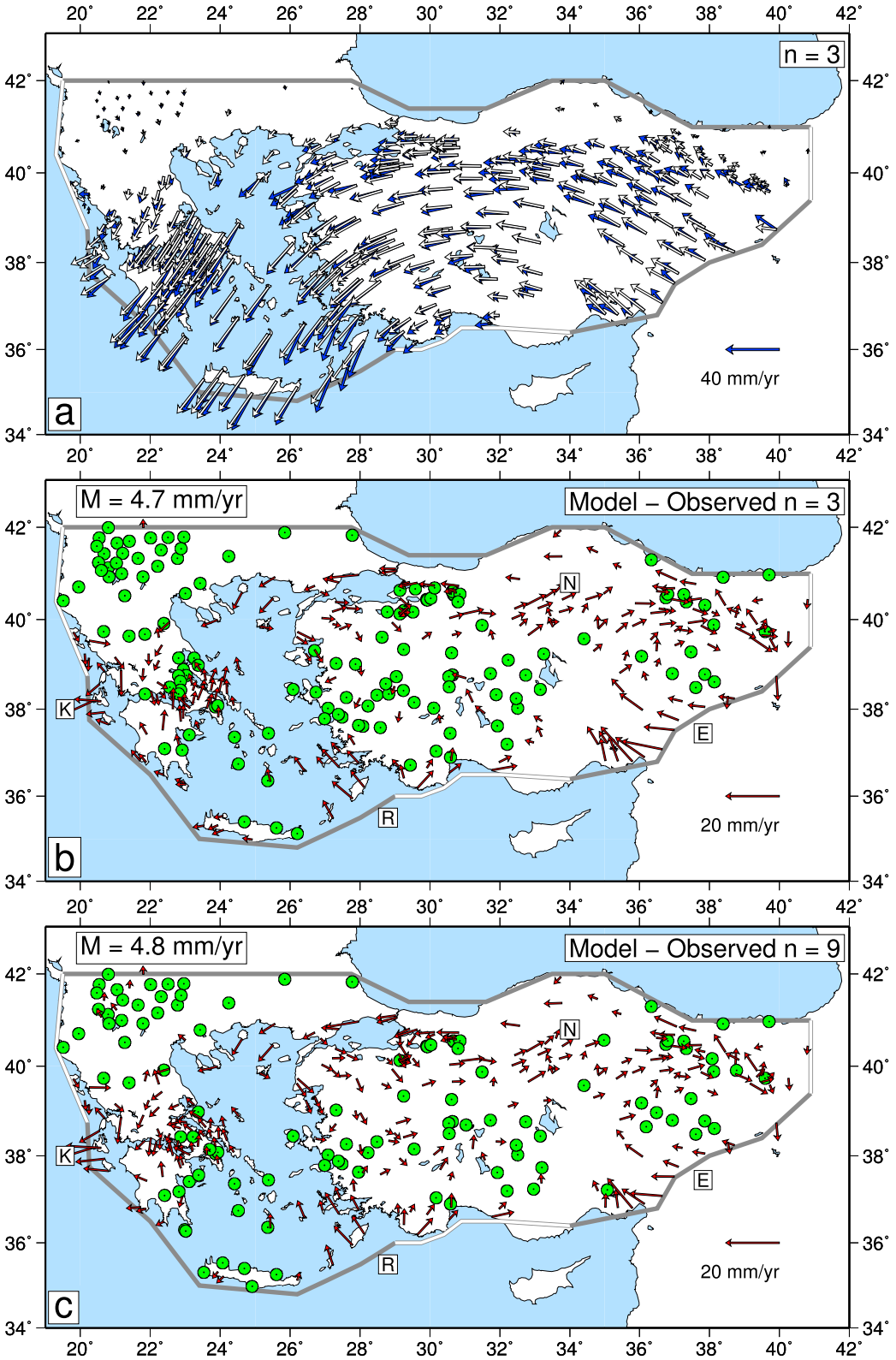

Figure 6. Best-fitting solutions for three-parameter calculations with $n = 3$ and 9 (section 5.2). (a) Best-fitting solution for $n = 3$. Blue arrows show the observed GPS velocities (Figure 2) and white arrows show model velocities. Red arrows show differences between the GPS velocities and the best-fitting three-parameter calculations with (b) $n = 3$ and (c) $n = 9$. Misfits are shown as (model minus observation). GPS sites for which the magnitude of the misfit is lower than 3 mm/yr are shown by green circles.

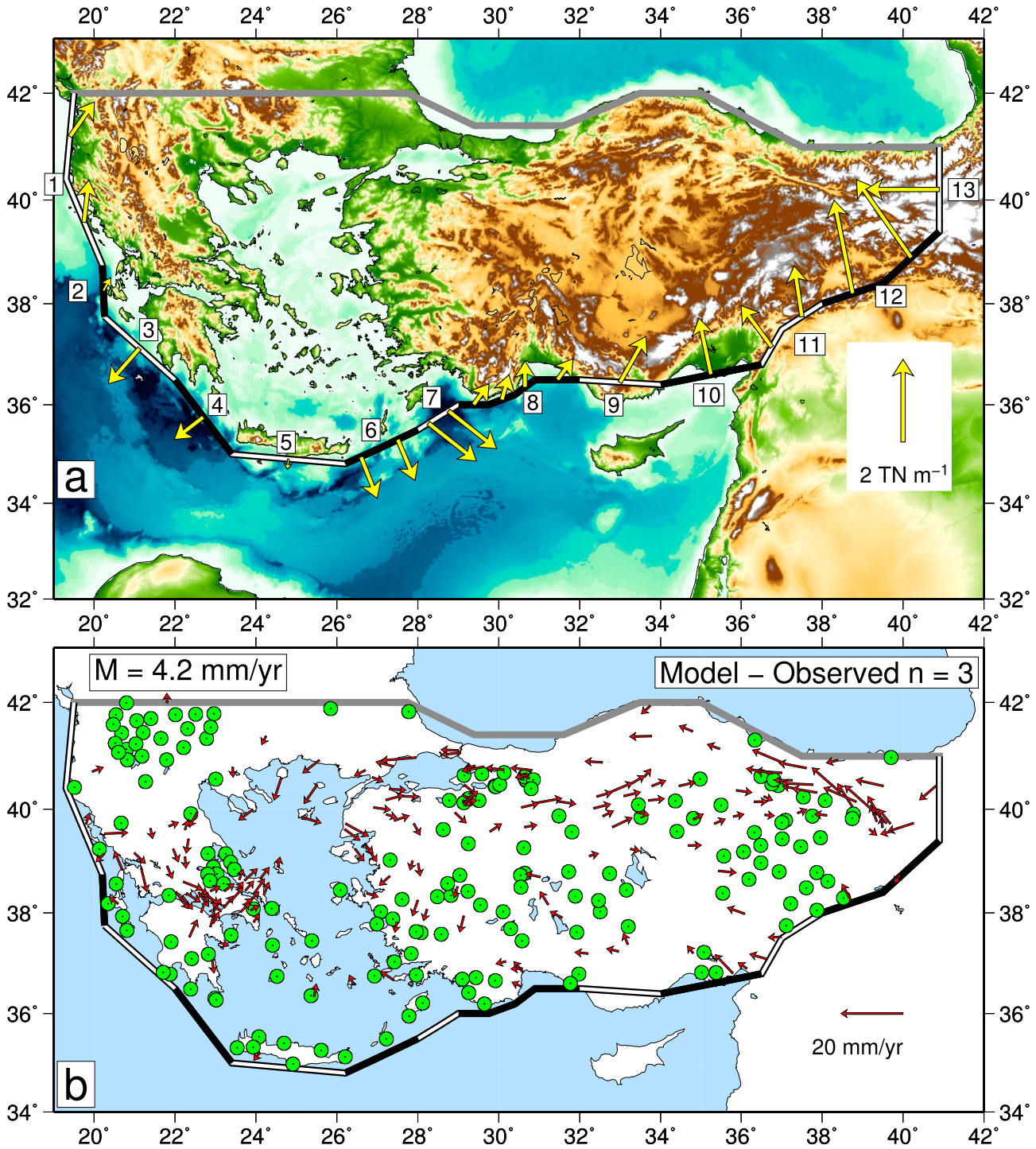

Figure 7. Calculation with separate boundary forces applied to 13 segments of boundary along the south and west of the domain (section 5.4) for a sheet with $n = 3$; B is 5.5×10^{11} Pa $s^{1/3}$. (a) Boundary conditions on grey lines are as in Figure 3b. Alternating black and white lines show the 13 boundary segments on which tangential and normal forces (yellow arrows, scale at right) are specified (Table 3). Where segments change strike along their lengths, vectors of the same magnitude but differing orientations are shown for each subsegment.

Table 3. Values of Forces per Unit Length on Boundary Segments Shown in Figure 7[a]

Segment Number	Normal Force TN m^{-1}	Tangential Force TN m^{-1}
1	−0.51	−0.89
2	−0.19	−0.32
3	1.14	0.00
4	0.89	0.00
5	0.25	0.00
6	1.08	−0.06
7	1.40	0.51
8	−0.51	0.38
9	−1.14	0.57
10	−1.40	0.00
11	−1.14	0.51
12	−2.29	0.32
13	−1.78	0.00

[a]Positive normal force corresponds to an extensional deviatoric stress at the boundary; positive tangential force corresponds to an applied sinistral shear.

adds complexity to the pattern of strain rate near the boundary, but deformation in the interior still responds principally to the long-wavelength features of the boundary conditions. To illustrate these considerations, we divided segments B–F of the boundary to the calculation domain into 13 smaller segments (Figure 7); there are only about 60 GPS observations in locations that are sensitive to these short boundary segments, so we do not consider subdivision at any finer scale. We adjusted the normal and tangential forces per unit length on those segments by trial and error until the magnitudes of misfits near each boundary segment become comparable with those in the interior, obtaining a solution (Figure 7 and Table 3) that has an RMS misfit of 4.3 mm/yr. Thus we show that misfits near the boundaries may plausibly be accounted for by minor adjustments to boundary conditions.

5.5. Lateral Heterogeneity

The misfit vectors in northern Anatolia (N in Figures 6b and 6c) show a more diffuse right-lateral shear in this region than is observed, suggesting that it is reasonable to investigate the additional complexity of a localized weak zone. We introduce the parameter B', which is the ratio of B within the weak zone to B in the rest of the sheet. We chose the shape of the weak zone to follow the North Anatolian Fault and its extension through the Sea of Marmara and into the North Aegean Trough (Figure 8) and carried out calculations for $n = 3$ and $n = 9$ in which B' varied between 1 and 0.1 in steps of 0.05, and Γ_W and $-\Gamma_E$ varied between 0 and 5 TN m^{-1}. With $n = 3$ the minimum misfit of 3.9 mm/yr is found with $B' = 0.45$; with $n = 9$, the minimum misfit of 4.4 mm/yr is found with $B' = 0.8$. It can be seen that most of the reductions in misfits, in comparison with the homogeneous calculations, arise from improved fit to observed velocities in the north of Anatolia (compare Figures 6b and 6c with Figures 8a and 8b).

Trades-off clearly exist between the value of B' and the width of the weak zone, and others can arise if aspects of the GPE distribution are incorrectly assigned. For example, because the dynamics is dominated by the balance between east-west gradients of GPE and gradients of deviatoric stress (sections 4 and A1), there would be a trade-off in misfits within Central Anatolia between those resulting from a decreased tangential force per unit length on its northern edge and those resulting from an increased west-to-east gradient in GPE across the region. Equally, strengthening or weakening the lithosphere near a particular boundary segment would, correspondingly, increase or decrease strain rates there, so that the reduction in misfits obtained by specifying a complex set of boundary forces (section 5.4) might alternatively have been obtained by multiple local adjustments to B [e.g., *Özeren and Holt*, 2010, Figure 10].

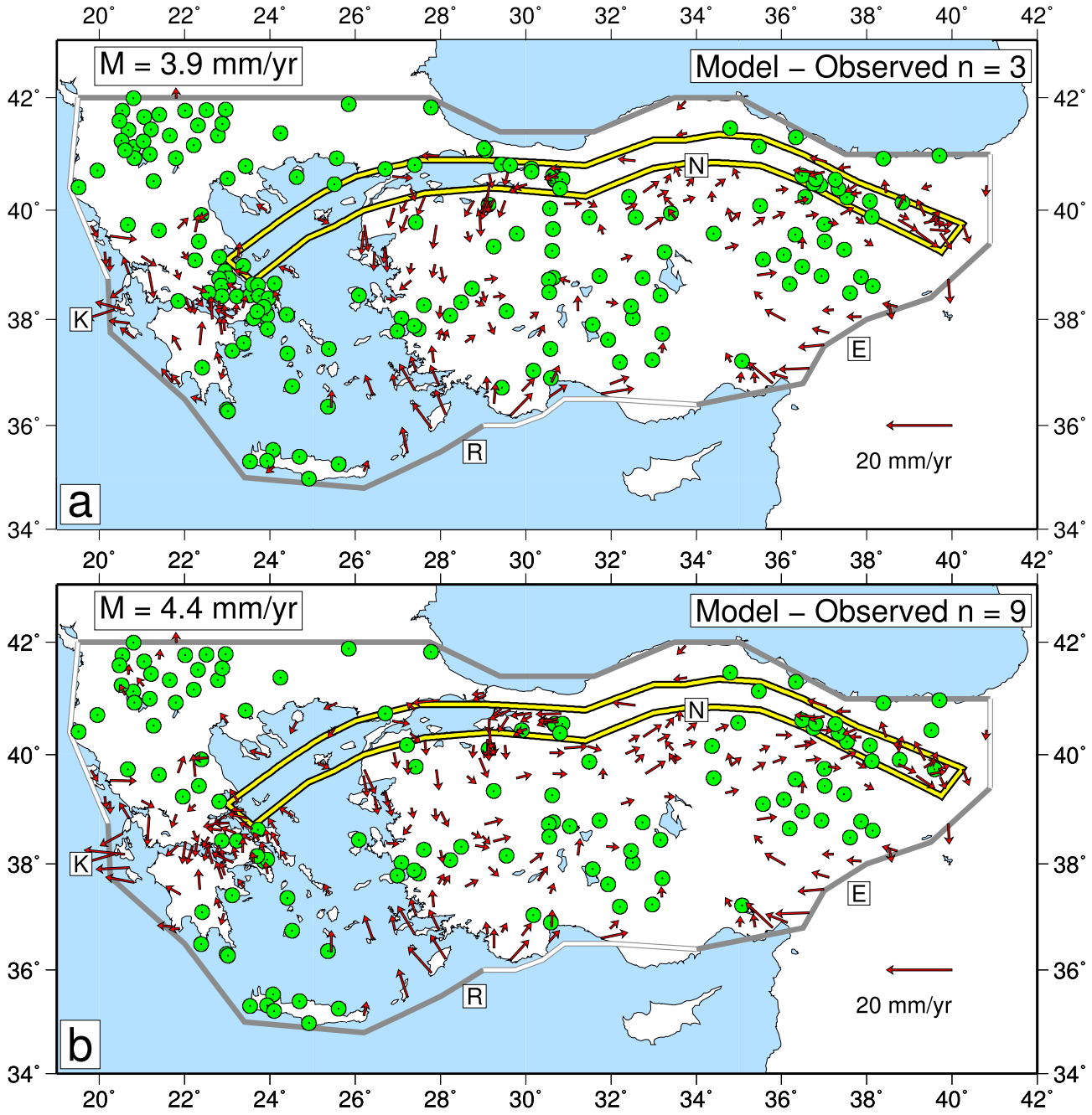

Figure 8. Misfits between observed velocities and calculations that include a weak region (outlined in yellow). (a) $n = 3$; $\Gamma_W = 1$ TN m^{-1}; $\Gamma_E = -1.6$ TN m^{-1}; $B' = 0.45$ within region outlined in yellow. (b) $n = 9$; $\Gamma_W = 1.6$ TN m^{-1}; $\Gamma_E = -2.1$ TN m^{-1}; $B' = 0.8$ within region outlined in yellow.

Removal of the simplifying assumption of laterally invariant material properties opens up a parameter space that is infeasible to explore systematically; the solutions of Figures 7 and 8 should therefore be regarded as illustrative, not definitive.

6. Tectonic Implications

We examine the implications of our analysis for the tectonics of the region, using the best-fitting solutions for the three-parameter calculations with $n = 3$ and 9 (Figure 6) and for the solution with multiple boundary segments and uniform B (Figure 7).

6.1. Boundary Forces

The best-fitting solutions for the calculations with spatially invariant rheology and $n > 1$ (Table 2) give a value for Γ_E, the compressional force per unit length at the eastern boundary (segment E, Figure 3b) between −2.25 and −1.5 TN m^{-1}, and the best-fitting (extensional) forces per unit length on the Hellenic boundary segment (C, Figure 3b) are between 0.6 and 1.6 TN m^{-1}. These estimates are consistent with those made by *Özeren and Holt* [2010] and by *Cianetti et al.* [2001]; we disagree, however, with these authors about the origin of these forces. *Özeren and Holt* [2010] refer to the forces at the Hellenic plate boundary as the result of "slab rollback," while *Cianetti et al.* [2001] refer to them as "trench suck force." If terms such as these have a dynamical meaning, it is that the negative buoyancy of the slab causes the normal stress acting on this boundary to be more tensional than would be expected from the lithostatic stress arising simply from the GPE of the external Nubian lithosphere [e.g., *Le Pichon*, 1982; *Molnar and Atwater*, 1978].

The best-fitting forces per unit length Γ_E and Γ_W are remarkably close to those expected from the GPE of isostatically balanced columns at the boundaries (a condition that is equivalent to $\Delta\Gamma_W$ and $\Delta\Gamma_E$ being small in the analytical approximation discussed in section 4). Smoothed surface heights in eastern Turkey reach 1500 to 2000 m (Figure 3a); the GPE associated with this range of heights is between 1.5 and 2 TN m^{-1} (equation (5)), which is consistent with the range obtained for Γ_E (Table 2). The GPE of ocean floor to the south of the Hellenic plate boundary is about 2 TN m^{-1} lower than that of our reference column of continental lithosphere [e.g., *Le Pichon*, 1982], so the range of 1 to 2 TN m^{-1} obtained for Γ_W (Table 2) suggests that, if anything, the state of stress at the Hellenic plate boundary is more compressional than would be expected from the GPE contrast alone.

The southward migration relative to Eurasia of the Nubian-Aegean boundary is a kinematic consequence of extension within the southern Aegean. "Slab rollback" is often inferred to accompany such "trench retreat"; forces associated with this process, and with more general flows in the upper mantle, have been suggested to cause deformation of Anatolia and the Aegean [e.g., *Faccenna et al.*, 2014; *Le Pichon and Kreemer*, 2010; *Royden*, 1993]. However, a physical model that includes only stresses associated with lateral variations in internal density structure of the lithosphere explains both the magnitudes and spatial variation of the observed velocity field, and we suggest that tractions caused by flow in the upper mantle exert only a minor influence on the deformation of the lithosphere in this region.

6.2. Strain Rates

We calculated a strain rate field from the GPS observations using the method of *Shen et al.* [2015], in which the horizontal velocity gradients are estimated at a set of regularly spaced grid points from the weighted GPS velocities by least squares inversion. The weight on each observation is the product of the area of the Voronoi cell occupied by the site and a Gaussian weight, $\exp\left(-R_{ij}^2/D_j^2\right)$, where R_{ij} is the distance of site i from grid point j. The smoothing distances, D_j, are chosen so that the total weight of observations on each grid point is the same. A weight of $W_T = 36$, in the notation of *Shen et al.* [2015], gives a median smoothing distance of 100 km, roughly the thickness of the lithosphere.

We first make quantitative comparisons between measures of the observed strain rate field and that of the best-fitting three-parameter calculation with $n = 3$; comparisons with the solutions for $n = 9$ and for the 13-segment boundary conditions yield similar results. Figure 9a superimposes the principal axes of strain rate derived from the GPS observations on the second invariant of the strain rate tensor (equation (2)) computed for the solution of Figures 6a and 6b. Calculated strain rates range from lower than 5 to over 150 nanostrain per year, and the geographical regions in which GPS observations show high and low strain rate correspond closely to the equivalent regions in the finite element calculations. At 202 out of the 323 locations for which strain rates are determined from the velocity measurements, the calculated and observed rates agree to within a factor of 2 (Figure 9b). The range in azimuths of the observed principal horizontal axes of compression is about 120° (Figure 9c). At 189 out of the 323 locations the calculated and observed azimuths agree to within 20°; at most of the sites where the disagreement is greater than 20° the strain rates are lower than 10 nanostrain/yr, as shown by the colors of the symbols in Figure 9.

Figure 10 compares the distribution of second invariant of the strain rate (equation (2)) derived from the GPS observations (section 4) with those of the best-fitting calculations for $n = 3$ and 9 (Figure 6) and of the calculation with multiple boundary segments (Figure 7). In the observations, a narrow band of high strain rate runs from south of the Black Sea, through the North Aegean Trough, and through central Greece. The presence of an equivalent narrow zone in the calculations reflects the property of a thin viscous sheet that the width of

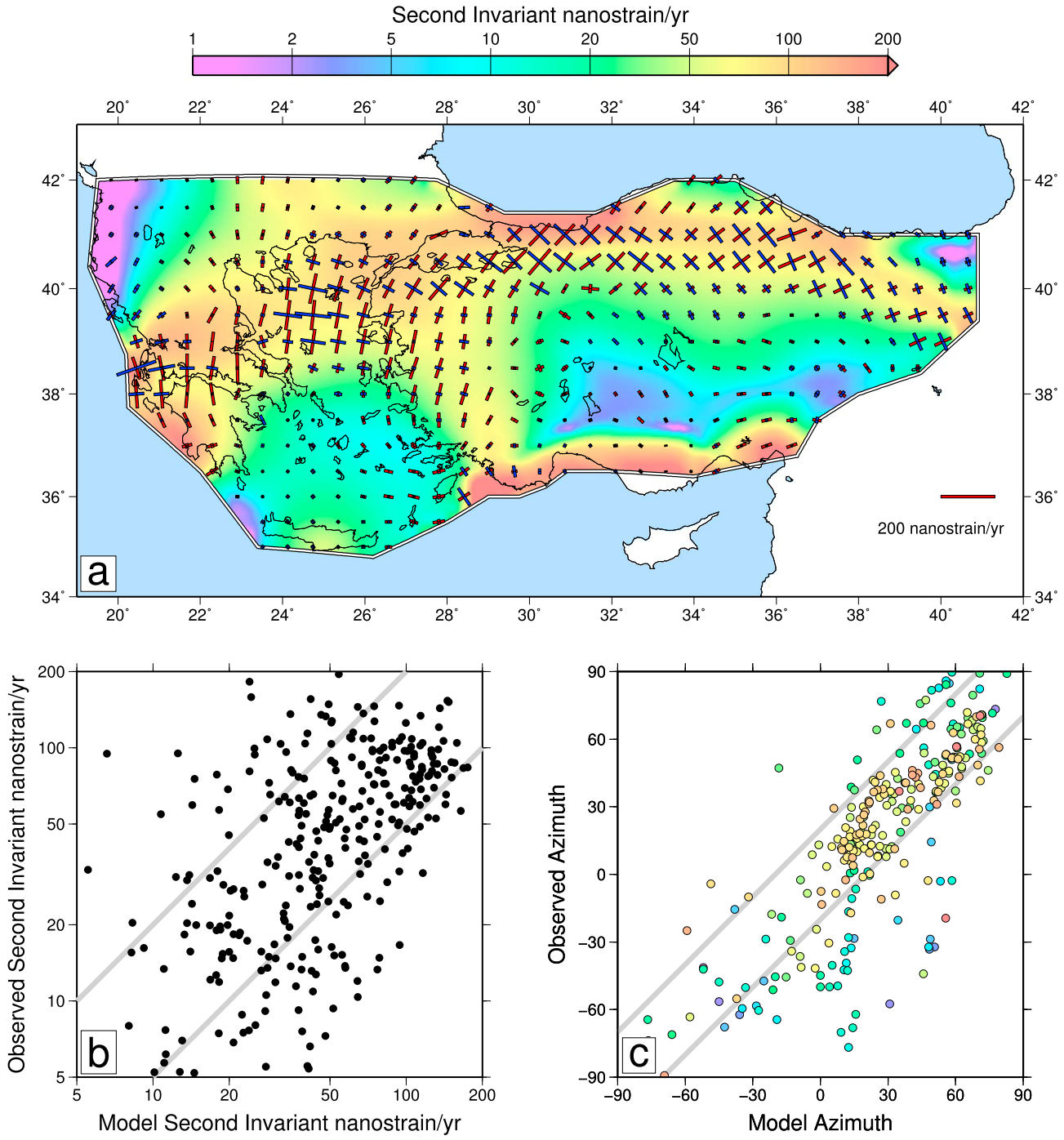

Figure 9. Comparison between observed and model strain rates. (a) Colors show the field of the second invariant of the strain rate tensor for the solution with $n = 3$ and constant B (Figures 6a and 6b); superimposed crosses show the orientations and magnitudes of the principal axes of strain rate model from the GPS velocities, as described in section 6.2. (b) Comparison between observed and model values of the second invariant of the strain rate tensor (equation (2)) at the location of each of the cross symbols in Figure 9a. Gray lines delineate the region in which model values are within a factor of 2 of the observed values. (c) Comparison between the azimuths of the principal horizontal axis of extension at the location of each of the cross symbols in Figure 9a and the azimuths of the same axes in the model deformation field. Symbols are colored according to the magnitude of the second invariant of strain rate in the best-fitting model calculation, at the geographical location of the observation. Gray lines delineate the region in which model azimuths are within 20° of the observed azimuths.

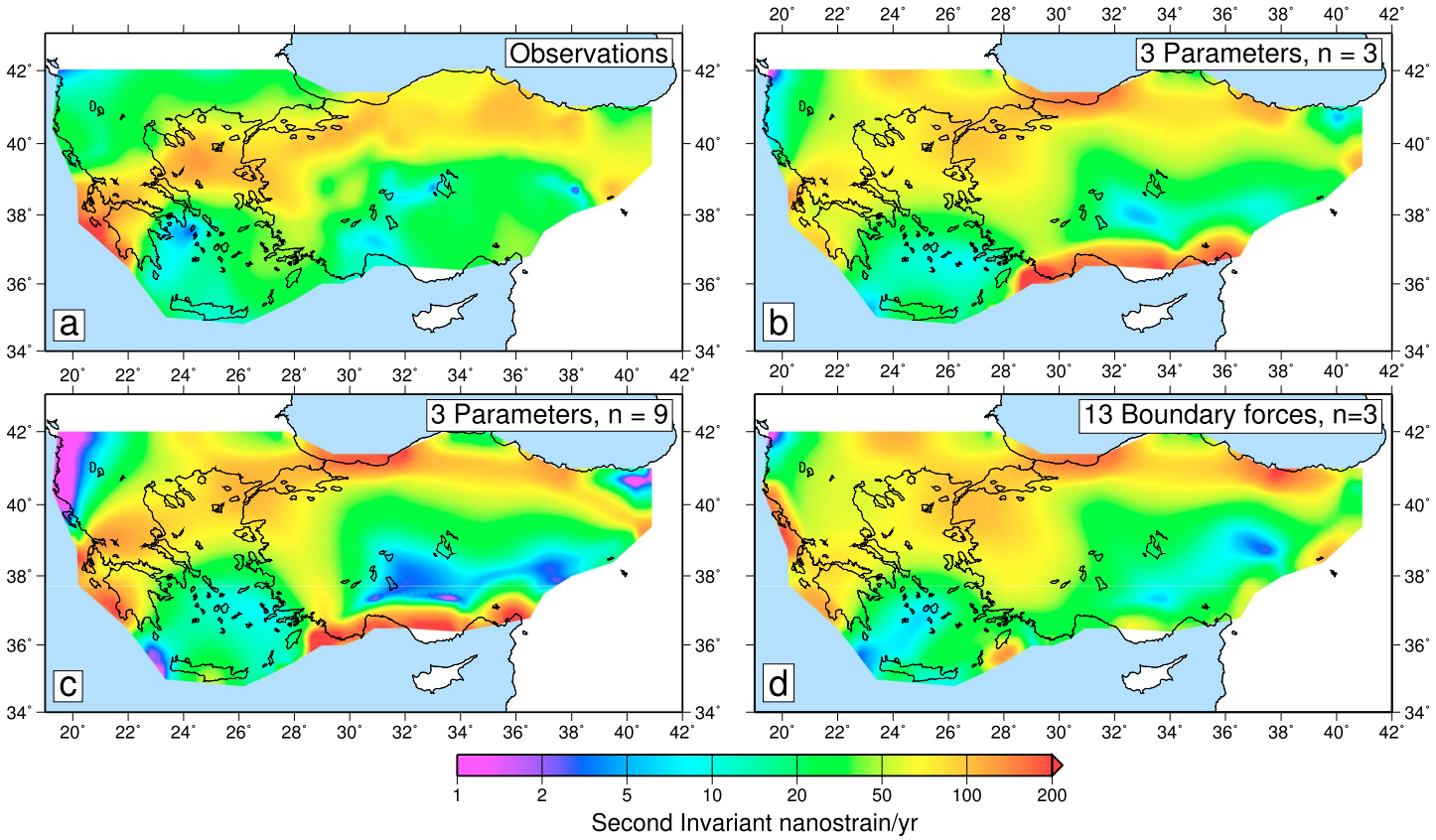

Figure 10. Observed and model fields of the second invariant of strain rate ($\dot{E}$, equation (2)). (a) Colors show the magnitude of $\dot{E}$ calculated from the GPS velocities, as described in section 6.2. (b) $\dot{E}$ for the best-fitting solution for the three-parameter calculations with $n = 3$ (Figure 6a). (c) as for (b), for the best-fitting solution for the three-parameter calculations with $n = 9$ (Figure 6c). (d) as for (b) for the calculation with 13 boundary forces (Figure 7).

a shear zone associated with a strike-slip boundary is much narrower than the length of the boundary itself (*England et al.* [1985] and see section 3.2). The greater is n, the greater is the decrease of viscosity with strain rate; the calculation for $n = 9$ shows a narrower band of high strain rate than that for $n = 3$.

The observed regions of low strain rate in eastern Anatolia and near the Hellenic plate boundary (Figure 10a) are also seen as regions of low strain rate in the calculations (Figures 10b–10d). Strain rates are low here because deviatoric stresses are low. The compressional force per unit length, Γ_E, applied at the eastern boundary is balanced by the high GPE of the lithosphere near the boundary, with eastern Turkey transmitting the plate boundary forces to the interior of Anatolia, in the same way that the elevated Tibetan plateau transmits the compressional force from India to the interior of Asia [*Molnar and Tapponnier*, 1978]. Equally, the extensional force per unit length at the Hellenic plate boundary is transmitted, through the low-GPE lithosphere of the southern Aegean, to the central and northern Aegean, and the adjacent parts of Greece and Turkey.

The horizontal divergence of the velocity field, $(\partial u_x/\partial x + \partial u_y/\partial y = -\dot{\varepsilon}_{zz})$ represents the rate of thickening or thinning of the lithosphere. The observed pattern of divergence shows horizontal extension over most of central Anatolia and all of western Turkey, Greece, and the Aegean Sea, with the highest rates of extension occurring in a horseshoe-shaped region surrounding the Aegean Sea (Figure 11a). This pattern is also seen in the calculations. The overall pattern of extension results from the contrast in GPE between those regions and the Nubian ocean floor to the south (section 6.1). Because the GPE on the margins of the Aegean Sea is higher than within it, rates of extension on the margins are correspondingly higher.

We emphasize that the extension in central Greece results from the contrast in GPE between this region and its surroundings. It has been suggested that the extension is enhanced by propagation of the North Anatolian Fault into the region [e.g., *Armijo et al.*, 1996, 1999, 2003; *Flerit et al.*, 2004]. This suggestion provides, however, no explanation for the equally prominent extensional deformation in the other locations of high relative GPE

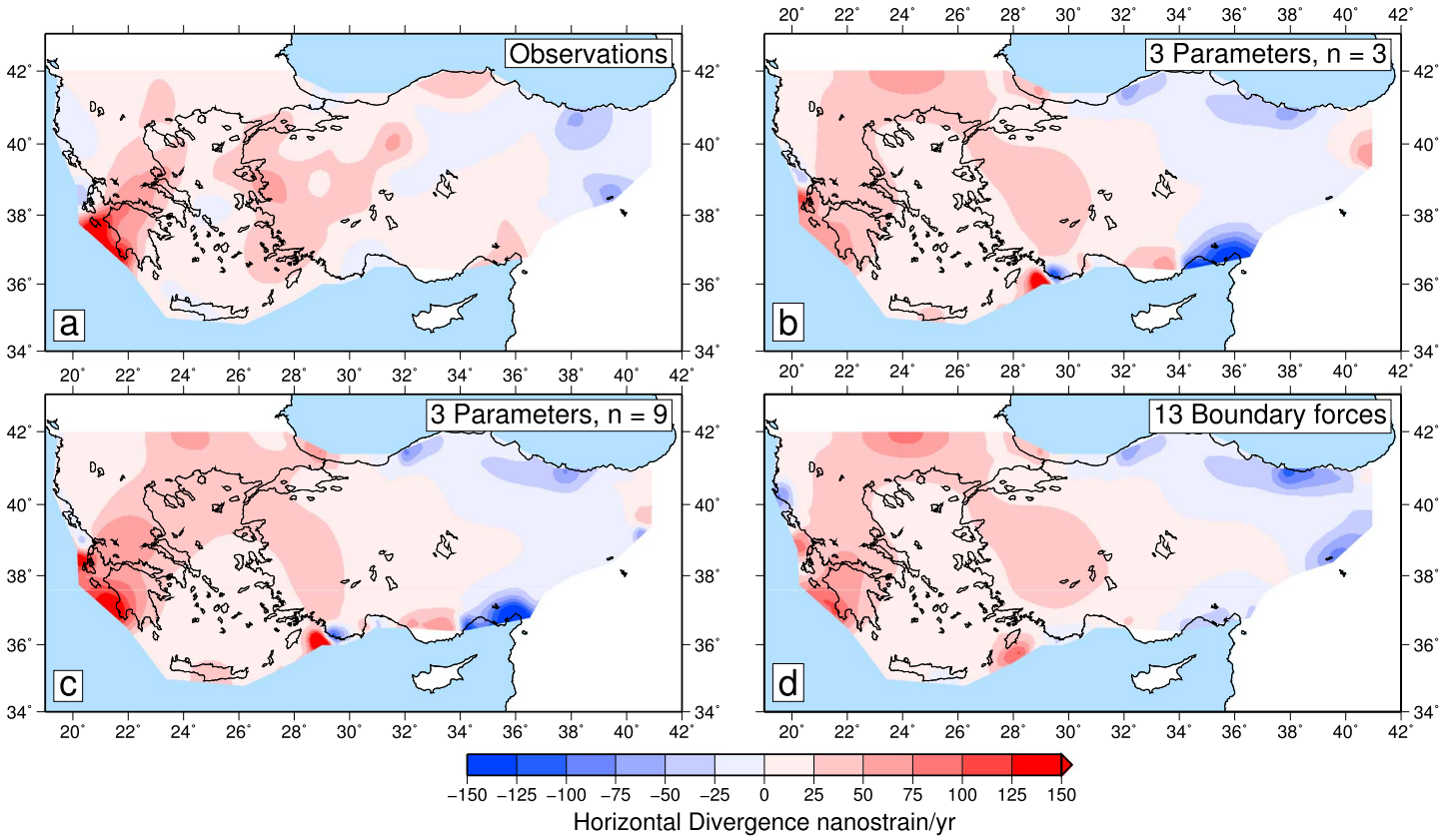

Figure 11. Observed and model fields of divergence of the horizontal velocity field. (a) Colors show the horizontal divergence calculated from the GPS velocities, as described in section 6.2; reds correspond to horizontal extension, blues to contraction. (b) Divergence for the best-fitting solution for the three-parameter calculations with $n = 3$ (Figure 6a). (c) as for (b), for the best-fitting solution for the three-parameter calculations with $n = 9$ (Figure 6c). (d) Same as Figure 9b but for the calculation with 13 boundary forces (Figure 7).

that surround the Aegean (see discussion of Figure 11). Our calculations with a homogeneous lithosphere are consistent with the strain rates derived from GPS, which show north-south extension in central Greece with negligible horizontal simple shear (Figure 9a), and with the dominance of normal faulting and absence of strike-slip faulting in the region (Figure 1) (see also *Floyd et al.* [2010], *Jackson* [1994], and *Pérouse et al.* [2012]).

6.3. Quasi-Rigid Motion of Fluid Lithosphere

Whereas we have been able to account for the distribution of velocities and strain rates in Greece and Turkey with a lithosphere that has spatially invariant physical properties (equation (1), with constant B), others have argued that the regions of low strain rate in the Southern Aegean and Central Anatolia (Figure 10a) represent strong inclusions or "microplates" [e.g., *Cianetti et al.*, 2001; *Fischer*, 2006; *Nyst and Thatcher*, 2004; *Le Pichon and Kreemer*, 2010; *Reilinger et al.*, 2006]. These two points of view may be reconciled by the recognition that any piece of lithosphere that is in a state of lower deviatoric stress than its surroundings will both deform more slowly and, by equation (3), have a higher effective viscosity.

Our calculations show high-viscosity regions, bordered by the yellow lines in Figure 12, which correspond to the Southern Aegean and parts of Southern and Central Anatolia. The high effective viscosity of these regions is entirely the consequence of the low deviatoric stresses acting within them. The GPS velocities within the corresponding geographical regions are fit by a rigid-body rotation with RMS residuals of 2.5 mm/yr (Anatolia) and 1.7 mm/yr (South Aegean) (Table 4). We found the rigid-body rotations that best fit the calculated velocities within these regions for the solutions with laterally invariant material properties and $n = 3$ and 9. The RMS residuals to these fits are, for each region, smaller than the misfits of the GPS vectors (Table 4), demonstrating that regions of plate-like behavior can arise naturally in the deformation of a lithosphere with power law rheology, without the need to impose lateral variation in material properties.

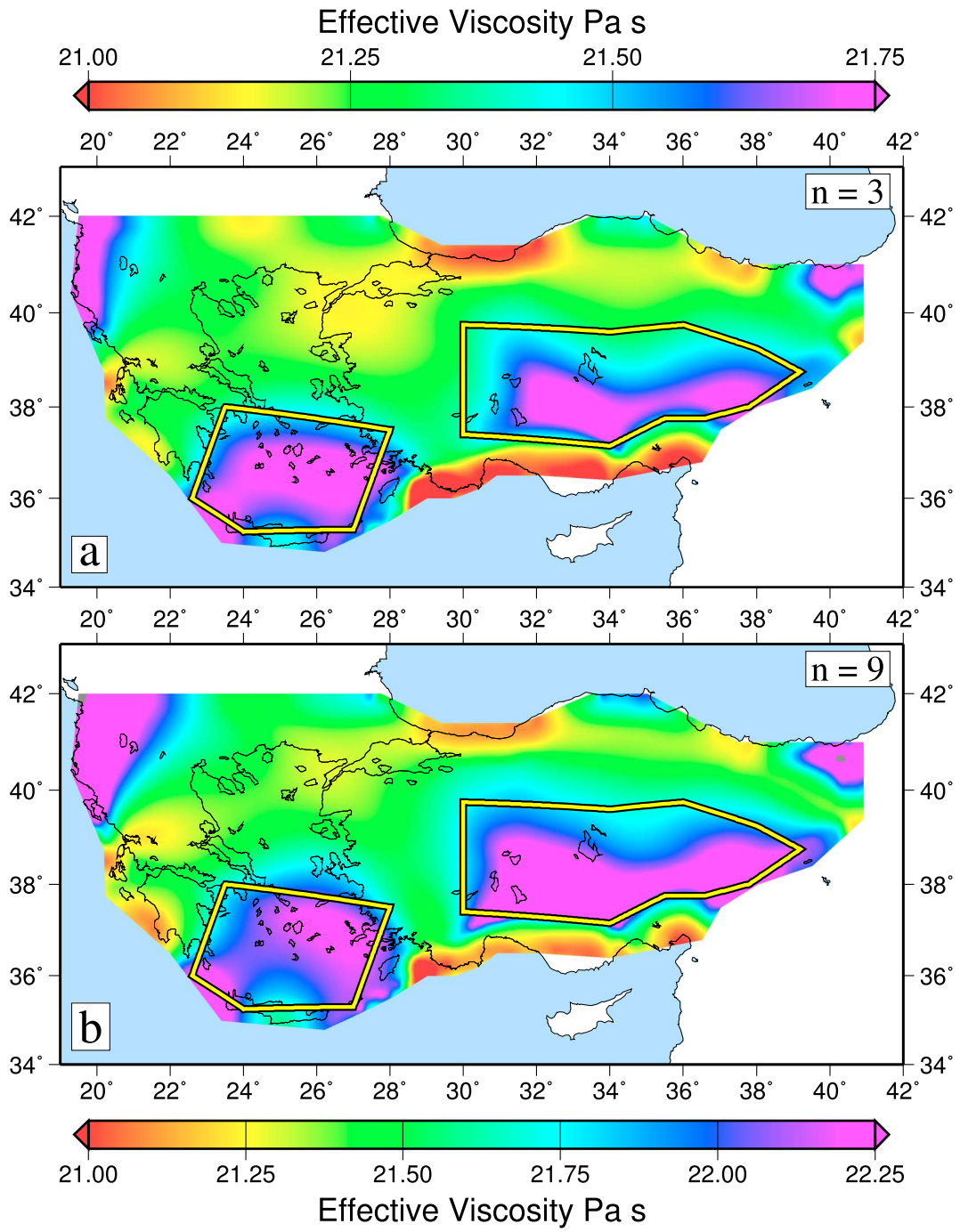

Figure 12. Model distributions of effective viscosity (η_{eff}, equation (3)) for the best-fitting solutions for the homogeneous sheet with (a) $n = 3$ and (b) 9 (Figure 6). Yellow lines show regions of high-viscosity fluid for which angular velocities are calculated, as though they were rigid bodies (Table 4).

6.4. Active Faulting and Seismicity

It is reasonable to ask whether the consistency between calculations and GPS observations spanning one or two decades extends to measures of the long-term geological strain such as deformation of crust by slip on faults. Adoption of the thin-sheet model to interpret GPS measurements of the Earth's surface motion carries the assumption that stresses associated with the deformation of the lower lithosphere are large enough to

Table 4. Angular Velocities for Central Anatolia and the Southern Aegean Calculated From GPS Observations and From the Solutions for the Deformation of a Homogeneous Sheet With $n = 3$ and 9[a]

	Longitude	Latitude	Rate (°/Myr)	RMS Misfit (mm/yr)
		Central Anatolia		
GPS	32.8°E	30.64°N	1.24	2.5
$n = 3$	31.4°E	29.4°N	1.1	2.4
$n = 9$	31.5°E	30.1°N	1.1	2.1
		South Aegean		
GPS	140.8°E	−45.3°N	0.39	1.7
$n = 3$	88.3°E	−27.4°N	0.28	1.0
$n = 9$	55.0°E	10.8° N	0.45	0.9

[a]The angular velocity that provides the best fit to the observed GPS velocities or to the calculated velocities, within the regions defined in Figure 12, is found by least squares regression (RMS misfit in fourth column).

cause matching deformation in the upper crust. Under that assumption, the expected style of deformation in the seismogenic upper crust is determined by the ratio of the principal horizontal strain rates, $\dot{\varepsilon}_1$ and $\dot{\varepsilon}_2$. The quantity

$$p = \frac{3}{4} + \frac{1}{\pi} \arctan\left(\frac{\dot{\varepsilon}_2}{\dot{\varepsilon}_1}\right) \tag{11}$$

indicates the expected style of surficial faulting [*Houseman and England*, 1986; *Gordon and Houseman*, 2015]. When $0 \leq p \leq 0.25$ reverse faulting only is predicted (RR, Figure 13). When $0.25 \leq p \leq 0.5$ there is reverse faulting plus subsidiary strike slip (RS) or strike slip plus subsidiary reverse faulting (SR), with the transition between RS and SR taking place where $p = 0.375$. Pure strike-slip faulting occurs when $p = 0.5$ and the transitions from strike slip with subsidiary normal faulting (SN) to normal faulting with subsidiary strike slip (NS) and from NS to NN take place at $p = 0.625$ and $p = 0.75$ (Figure 13).

Figure 13 compares the distributions of active faulting [*Goldsworthy and Jackson*, 2000, 2001; *Goldsworthy et al.*, 2002; *Şaroglu et al.*, 1992] and earthquakes [*Dziewonski et al.*, 1981; *Ekström et al.*, 2012; *McKenzie*, 1972; *Taymaz et al.*, 1991a, 1991b; *Jackson and McKenzie*, 1988; *Shaw and Jackson*, 2010] with the distribution of p derived from the solution with multiple boundary segments (Figure 7). Deformation above the subduction interface, which is delineated by thrust-faulting earthquakes whose focal planes dip more shallowly than 25° [*Shaw and Jackson*, 2010], is not treated by our formulation so earthquakes on and above this interface are excluded from the comparison.

Normal faulting is predicted to dominate (NS, NN, $p > 0.625$, Figure 13) in Greece, most of the southern Aegean, and southwest Anatolia. The active faults in the regions where $p > 0.625$ are predominantly normal (Figure 13a) and 148 out of the 233 normal-faulting earthquakes were in these regions (Figure 13b and Table 5). The main regions in which strike-slip faulting is predicted to dominate (SR, SN, $0.375 < p < 0.625$, Figure 13) correspond to the northern Aegean, westernmost Turkey, the Sea of Marmara, north Anatolia, and eastern Anatolia. These regions exhibit strike-slip faulting, with some normal faulting in westernmost Turkey (Figure 13a), and 88 out of the 114 earthquakes with strike-slip focal mechanisms occurred within the regions for which $0.375 < p < 0.625$ (Figure 13c and Table 5).

The principal discrepancy in this comparison appears to lie in the absence of reverse-faulting earthquakes in regions RS and SR on Figure 13c. Note, however, that only 18 earthquakes lie in the region for which $p < 0.375$, whereas there were 329 in the regions of normal-plus strike-slip faulting (Table 5). Furthermore, some of the strike-slip earthquakes exhibit an oblique component that implies a component of vertical thickening, consistent with $p < 0.5$, and many of the pre-1960 earthquakes were assigned a pure strike-slip mechanism, in the absence of strong constraint from first-motion observations.

The agreement between the observed and calculated styles of deformation (Figure 13) implies that the seismogenic upper crust is weak enough to deform pervasively in response to the stresses arising from contrasts in GPE within the lithosphere. This implication is supported by the observation that the T axes of earthquakes

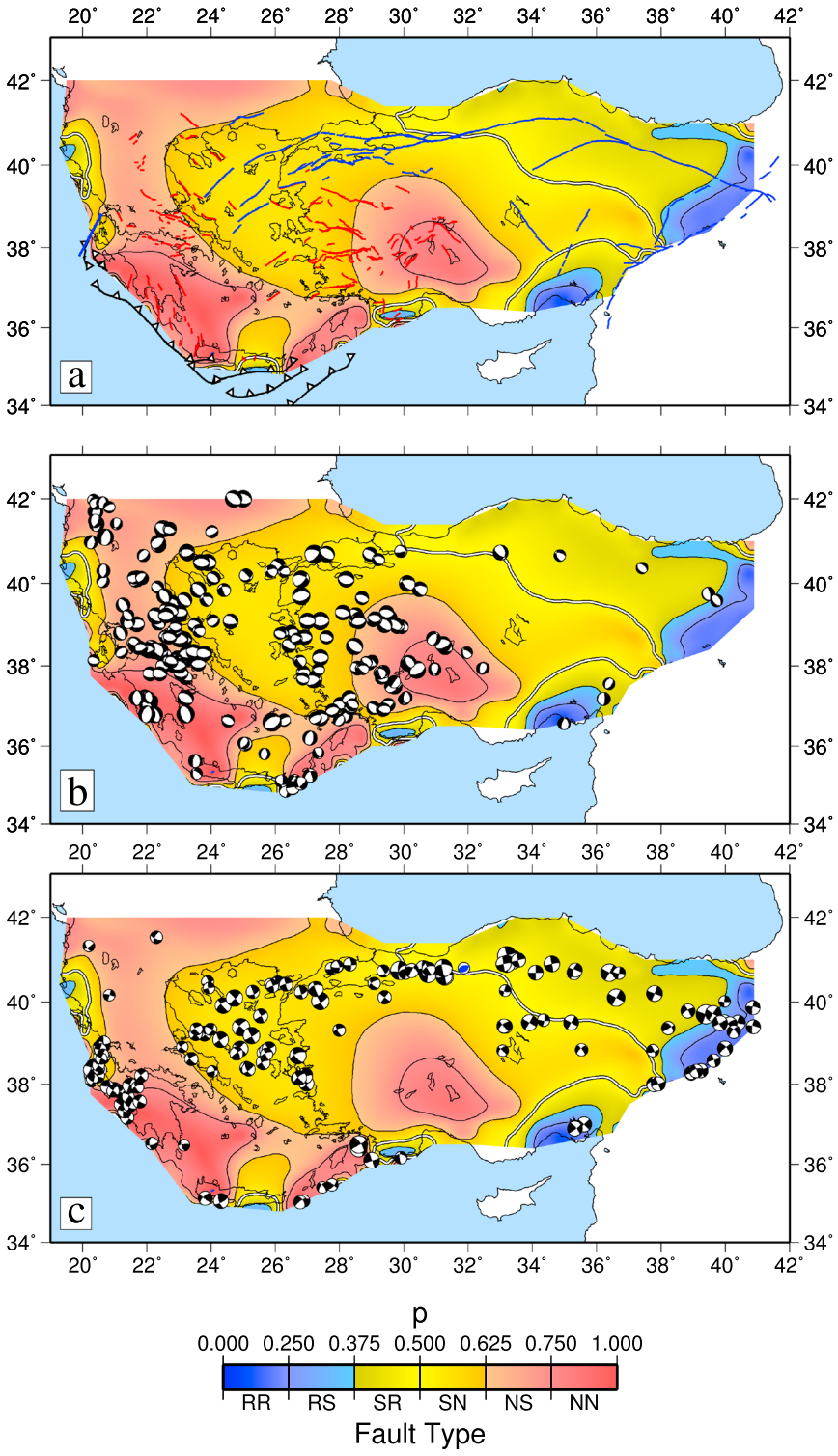

Figure 13. Predicted distributions of fault types for the calculation with 13 boundary forces (Figure 7) compared with observed distribution of faulting and earthquake focal mechanisms. Colors show the distribution of fault types predicted by the model strain rate field (equation (11), section 6.4); in the two-letter designations, N, S, R, refer to normal, strike-slip, and reverse faulting; the first letter refers to the type of faulting that accommodates the greater fraction of strain rate. The $p = 0.5$ contours are shown as double lines. (a) Active faults are shown in blue (strike slip) or red (normal) [*Goldsworthy and Jackson*, 2000, 2001; *Goldsworthy et al.*, 2002; *Şaroglu et al.*, 1992]. (b) Normal-faulting earthquakes of the region. (c) Strike-slip-faulting earthquakes of the region. Focal mechanisms from the GCMT catalog [*Dziewonski et al.*, 1981; *Ekström et al.*, 2012] and from *Jackson and McKenzie* [1988] and *Shaw and Jackson* [2010].

Table 5. Numbers of Normal-, Strike-Slip-, and Reverse-Faulting Earthquakes Within the Continental Lithosphere of Anatolia and the Aegean[a]

Predicted Dominant Fault Type	Number of Earthquakes		
	Normal	Strike Slip	Reverse
RR	1	10	0
RS	1	6	0
SR	6	21	1
SN	77	67	1
NS	124	7	0
NN	24	3	0

[a]Earthquakes are sorted by areas in which the calculations of Figure 13 indicate that different fault types should dominate the deformation (equation (11) and Figure 13). The earthquakes are separated into normal-, strike-slip-, or reverse-faulting events according to whether the smallest, intermediate, or greatest principal axis of their moment tensor is closest to vertical.

in Greece and western Turkey are aligned with the axes of principal elongation of the strain rate field derived from GPS [*Floyd et al.*, 2010, Figure 17]. This alignment holds regardless of size of the earthquake, or of whether it lies close to a postulated block boundary, again suggesting that the faults within the upper crust of the region are taking up a continuous field of deformation.

Many of the earthquakes in this region whose magnitudes exceed about 6 may confidently be associated with faults that show displacements of hundreds of meters to kilometers over Pliocene-to-Quaternary time [e.g., *Jackson*, 1994; *Goldsworthy and Jackson*, 2000, 2001; *Goldsworthy et al.*, 2002; *Şaroglu et al.*, 1992]. The agreement between the style of deformation shown by our calculations and the distribution of active faulting and earthquakes suggests that the Pliocene-to-present phase of deformation in the Aegean is explained by the same balance between gravitational potential energy and viscous stresses that governs the deformation field measured by GPS.

7. Conclusions

We have analyzed the deformation of Anatolia and the Aegean using a physical model that has three free parameters: the power law exponent n of the fluid lithosphere, Γ_E representing the force per unit length acting at the boundary between eastern Turkey and Arabia, and Γ_W representing the force per unit length acting at the boundary between Nubia and the Aegean. The simplicity of this model allows us to calculate velocity fields throughout the entire relevant parameter space. The best-fitting combinations of parameters account for over 90% of the variance in the GPS velocities (section 5.3). The three-parameter numerical experiments are supported by approximate analytical solutions that explain the scaling relations between tectonic velocities, gravitational potential energy of the lithosphere per unit area (GPE), and lithospheric rheology (sections 4 and A1).

The RMS misfit between model and observations may be reduced by allowing a more complex configuration of boundary condition (section 5.4) and by introducing a zone of lithospheric weakness in the region corresponding to the North Anatolian Fault and the North Aegean Trough (section 5.5). Although each of these complications is reasonable on geological grounds, we are mindful of von Neumann's aphorism that with four parameters he could fit an elephant and with a fifth he could make it wiggle its trunk [*Dyson*, 2004], and base our conclusions on the three-parameter calculations (Figure 6). As illustrated in Figures 10 and 11, the principal features of the simple solutions are retained in the more complex solution that we also consider.

Our analysis supports the conclusions of previous studies [e.g., *Hatzfeld et al.*, 1997; *Le Pichon*, 1982; *Le Pichon and Angelier*, 1979; *Martinod et al.*, 2000; *McKenzie*, 1972; *Métois et al.*, 2015; *Özeren and Holt*, 2010] that tectonic activity in Anatolia and the Aegean is explained by the balance between internal gradients of GPE within the continental lithosphere of the region and the deviatoric stresses required to deform the lithosphere.

Calculations in which deformation is forced solely by boundary tractions fit the observations significantly more poorly (RMS misfit ~7.5 mm/yr, Figure 5d).

The magnitudes of forces per unit length acting at the boundaries between Arabia and eastern Turkey (Γ_E) and between Nubia and the Aegean (Γ_W) are between 1 and 2 TN m^{-1} and are comparable with the GPE inferred for lithospheric columns external to these boundaries. We rule out significant contribution to the force balance of the Aegean from processes that are postulated under labels such as "slab pull," "slab roll-back," or "trench retreat." The influence of basal tractions on the lithosphere, due to convection in the mantle, is also likely to be minor in comparison with the influence of lateral gradients of GPE within the lithosphere (section 6.1).

The distributions of velocities and strain rates derived from GPS, of active faulting, and of the focal mechanisms of earthquakes are explained by the deformation of a homogeneous sheet with a rheology whose power law exponent, n, is 3 or higher (sections 6.2 and 6.4). Large regions of low strain rate, such as Anatolia and the southern Aegean, arise naturally as a result of the inverse dependence of the effective viscosity on the magnitude of the deviatoric stress for $n > 1$. These regions deform slowly because the deviatoric stresses acting upon them are lower and their effective viscosities are correspondingly higher (equation (3) and see section 6.3). For a homogeneous sheet with $n = 3$ the effective viscosity of the lithosphere lies between approximately 10^{22} Pa s at 10 nanostrain per year and 2×10^{21} Pa s at 100 nanostrain per year (Figures 10b and 12a). The effective viscosities for the sheet with $n = 9$ are respectively doubled and halved at the same strain rates (Figures 10c and 12b).

Although spatial variation in rheological properties of the lithosphere is not required in order to explain the first-order features of the deformation of the region, it is likely that the area around the North Anatolian fault and its extension into the Aegean is somewhat weaker than the rest of the region. The reduction in viscosity coefficient (B, equation (1)) that gives the best fit to GPS observations in this region is a factor of 50% for a lithosphere whose power law exponent, n, is 3 or 20% for $n = 9$ (section 5.5 and Figure 8).

Appendix A: Solution of Thin-Sheet Equations

A1. Analytical Solutions

A1.1. Flow of a Rectangular Newtonian Thin Sheet

The Cartesian form of the thin-sheet equation is

$$\begin{aligned} 2\frac{\partial\overline{\tau}_{xx}}{\partial x}+\frac{\partial\overline{\tau}_{yy}}{\partial x}+\frac{\partial\overline{\tau}_{xy}}{\partial y}&=\frac{1}{L}\frac{\partial\Gamma}{\partial x}\\ 2\frac{\partial\overline{\tau}_{yy}}{\partial y}+\frac{\partial\overline{\tau}_{xx}}{\partial y}+\frac{\partial\overline{\tau}_{xy}}{\partial x}&=\frac{1}{L}\frac{\partial\Gamma}{\partial y}\end{aligned} \tag{A1}$$

[*Bird and Piper*, 1980; *England and McKenzie*, 1983]. We treat the region of interest as a rectangular box ($0 < x < l$; $-w < y < w$, with the x direction being approximately eastward and the y direction being approximately northward: Figure 4). We neglect the y component of velocity and allow the GPE of the sheet to vary only in the x direction, with a constant gradient $\Delta\Gamma/l$, where $\Delta\Gamma$ represents the difference in GPE between Eastern Anatolia and the Southern Aegean. Equation (A1) then reduces to

$$2\frac{\partial\overline{\tau}_{xx}}{\partial x}+\frac{\partial\overline{\tau}_{xy}}{\partial y}=\frac{\Delta\Gamma}{Ll}. \tag{A2}$$

For a Newtonian fluid of constant viscosity η, equation (A2) with $u_y = 0$ becomes

$$\frac{\partial^2 u_x}{\partial x^2}+\frac{1}{4}\frac{\partial^2 u_x}{\partial y^2}=\frac{\Delta\Gamma}{4\eta Ll}, \tag{A3}$$

We set $u_x = 0$ on $y = \pm w$. On $x = 0$ we apply a normal force per unit length arising from the difference $\Delta\Gamma_W$ in GPE across the boundary (outside-inside). This condition requires that

$$\left.\frac{\partial u_x}{\partial x}\right|_{x=0}=-\frac{\Delta\Gamma_W}{4\eta L}. \tag{A4}$$

Similarly, we set

$$\left.\frac{\partial u_x}{\partial x}\right|_{x=l} = -\frac{\Delta\Gamma_E}{4\eta L}, \tag{A5}$$

where $\Delta\Gamma_E$ is the contrast in GPE across the boundary $x = l$ (again, outside-inside). With these boundary conditions, the solution to equation (A3) is

$$u_x = \frac{\Delta\Gamma w^2}{2\eta L l}\left(\frac{y^2}{w^2} - 1\right) + \frac{4w}{\pi^2\eta L}\sum_{n=0}^{\infty}\frac{(-1)^n}{(2n+1)^2}\frac{\cos\left(2c_n y\right)}{\sinh\left(c_n l\right)}\left(\Delta\Gamma_W \cosh\left(c_n(l-x)\right) - \Delta\Gamma_E \cosh\left(c_n x\right)\right) \tag{A6}$$

where

$$c_n = \frac{(2n+1)\pi}{4w} \tag{A7}$$

The maximum magnitude of (westward) velocity is at $x = 0$, $y = 0$; the scaling of this velocity, when GPE increases eastward and $\Delta\Gamma_W$ and $\Delta\Gamma_E$ are positive, is given approximately by retaining only the first term in the summation:

$$|u|_{\max} \sim \frac{\Delta\Gamma w^2}{2\eta L l} + \frac{4w}{\pi^2\eta L}\left(\frac{\Gamma_W}{\tanh\left(\pi l/(4w)\right)} - \frac{\Gamma_E}{\sinh\left(\pi l/(4w)\right)}\right). \tag{A8}$$

With $l \sim 1800$ km and $w \sim 300$ km, $\tanh\left(\pi l/(4w)\right) \sim 1$ and $\sinh\left(\pi l/(4w)\right) \sim 50$,

$$|u|_{\max} \sim \frac{\Delta\Gamma w^2}{2\eta L l} + \frac{4\Gamma_W w}{\pi^2\eta L} \tag{A9}$$

A1.2. Approximate Solution for a Thin Sheet With Power Law Rheology

The first term in equation (A6), in which u_x is independent of x, describes flow in the thin sheet in response to the gradient in GPE along it, $\Delta\Gamma/l$. This expression is equivalent to that for fluid confined between two parallel planes and subjected to a constant pressure gradient (Poiseuille flow) [e.g., *Turcotte and Schubert*, 2014, p. 357] (see equation (A12)). The terms in the summation of equation (A6) represent the response of the sheet to the boundary conditions on $x = 0$ and $x = l$. The magnitude of each of these terms decays approximately exponentially with distance from the relevant boundary as may be seen, for example, by considering the first term arising from the boundary condition on $x = 0$ when $x \lesssim w$:

$$\frac{4\Delta\Gamma_W w}{\pi^2\eta L}\cos\left(\pi y/2w\right)\frac{\cosh\left(\pi(l-x)/4w\right)}{\sinh\left(\pi l/4w\right)} \sim \frac{4\Delta\Gamma_W w}{\pi^2\eta L}\cos\left(\pi y/2w\right)\exp\left(-\pi x/4w\right), \tag{A10}$$

with an equivalent relation for velocities associated with the boundary condition at $x = l$. The length scale for the decay is $4w/\pi$, which is close to the length scale given by the analysis of *England et al.* [1985] for the case of a Newtonian fluid (see section 3.2). In the configuration we consider here, $w \sim 300$ km and, as we show in Figure A1, the influence of the terms corresponding to the conditions on $x = 0$ and $x = l$ decreases by a factor of e within about 400 km of those boundaries. For a power law fluid, this length scale would be reduced by a factor of $\sqrt{n}$; recall that the length of the region we consider is $l \sim 1800$ km.

These considerations suggest an approximate solution for a power law fluid in which velocities close to the boundaries $x = 0, l$ are influenced by forces at those boundaries, but velocities distant from either boundary are described by Poiseuille flow forced by a constant internal gradient of GPE, $\Delta\Gamma/lL$, in the x direction. The equation for Poiseuille flow of a power law fluid described by equation (1) is

$$\frac{\partial\,\overline{\tau}_{xy}}{\partial y} = B\sqrt{2}^{\,(1/n-1)}\frac{\partial}{\partial y}\left(\left|\dot{\varepsilon}_{xy}\right|^{1/n-1}\dot{\varepsilon}_{xy}\right) = \frac{\Delta\Gamma}{lL}, \tag{A11}$$

where the quantity $\Delta\Gamma/lL$ is equivalent to the pressure gradient acting in the x direction in the conventional description of Poiseuille flow and

$$\dot{E} = \sqrt{2}\left|\dot{\varepsilon}_{xy}\right| = \frac{1}{\sqrt{2}}\left|\frac{\partial u_x}{\partial y}\right|$$

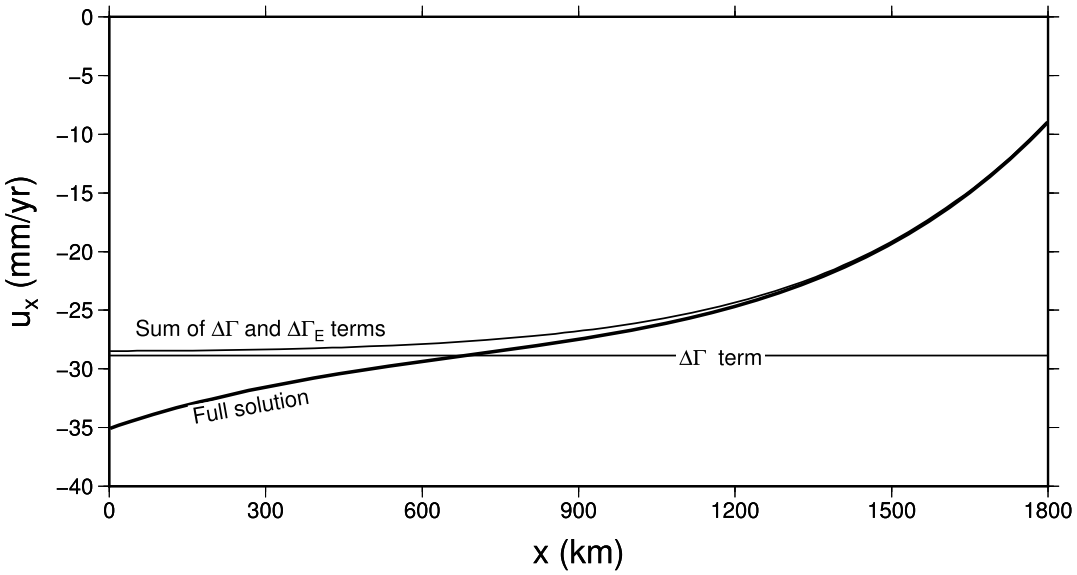

Figure A1. Components of the analytical solution for flow of a Newtonian viscous sheet in a box. The thick line shows the full solution (equation (A6)), with $l = 1800$ km, $w = 300$ km, $L = 100$ km. $\Delta\Gamma$, $\Delta\Gamma_W$, and $\Delta\Gamma_E$ were obtained by fitting equation (A6) to the observed velocities in Anatolia and the Aegean, as described in section 4 and Figure 4. The thin horizontal line (labeled "$\Delta\Gamma$ term") corresponds to the first term in equation (A6). The thin line labeled "Sum of $\Delta\Gamma$ and $\Delta\Gamma_E$ terms" adds the terms in the summation arising from the force $\Delta\Gamma_E$ on the eastern ($x = l$) boundary.

The solution to this equation, using the symmetry condition that $\partial u_x/\partial y = 0$ on $y = 0$, is

$$u_x = \Delta\Gamma\,|\Delta\Gamma|^{n-1}\,\frac{\sqrt{2}^{(n+1)}}{(n+1)}\left(\frac{w}{lLB}\right)^n\left(1-\left(\frac{y}{w}\right)^{(n+1)}\right)w. \tag{A12}$$

This result generalizes the solution of *Turcotte and Schubert* [2014, p. 357] to values of n other than even integers.

The maximum speed in this flow is on the center line, $y = 0$:

$$|u|_{\max} = \frac{\sqrt{2}^{(n+1)}}{(n+1)}\left(\frac{\Delta\Gamma\, w}{lLB}\right)^n w. \tag{A13}$$

A2. Numerical Solutions

The thin-sheet approximation assumes that vertical tractions on vertical planes may be neglected, so that density variations within the lithosphere are in local isostatic balance. Under this condition, the stress balance equation for creeping flow in spherical coordinates is

$$\begin{aligned}\frac{2}{r}\frac{\partial\,\overline{\tau}_{\theta\theta}}{\partial\,\theta}+\frac{1}{r}\frac{\partial\,\overline{\tau}_{\phi\phi}}{\partial\,\theta}+\frac{1}{r\sin\theta}\frac{\partial\,\overline{\tau}_{\theta\phi}}{\partial\,\phi}+\frac{\cot\theta}{r}\left(\overline{\tau}_{\theta\theta}-\overline{\tau}_{\phi\phi}\right)&=\frac{1}{rL}\frac{\partial\,\Gamma}{\partial\,\theta}\\ \frac{1}{r\sin\theta}\frac{\partial\,\overline{\tau}_{\theta\theta}}{\partial\,\phi}+\frac{2}{r\sin\theta}\frac{\partial\,\overline{\tau}_{\phi\phi}}{\partial\,\phi}+\frac{1}{r}\frac{\partial\,\overline{\tau}_{\theta\phi}}{\partial\,\theta}+\frac{2\cot\theta}{r}\overline{\tau}_{\theta\phi}&=\frac{1}{r\sin\theta L}\frac{\partial\,\Gamma}{\partial\,\phi}\end{aligned} \tag{A14}$$

where θ and ϕ are, respectively, the colatitude and the longitude (in radians) and r is the radial distance from the center of the Earth, L is the thickness of the lithosphere, and Γ is the gravitational potential energy per unit area of lithosphere (GPE) [*Bird and Piper*, 1980; *England and McKenzie*, 1983; *Gordon and Houseman*, 2015; *Houseman and England*, 1986].

The relevant components of the strain rate tensor are

$$\dot{\varepsilon}_{\theta\theta} = \frac{1}{r}\frac{\partial u_\theta}{\partial\theta} \tag{A15}$$

$$\dot{\varepsilon}_{\phi\phi} = \frac{1}{r\sin\theta}\frac{\partial u_\phi}{\partial\phi}+\frac{u_\theta}{r}\cot\theta \tag{A16}$$

$$\dot{\varepsilon}_{\theta\phi} = \frac{1}{2}\left(\frac{1}{r\sin\theta}\frac{\partial u_\theta}{\partial\phi} + \frac{1}{r}\frac{\partial u_\phi}{\partial\theta} - \frac{u_\phi}{r}\cot\theta\right) \tag{A17}$$

We nondimensionalize these equations using the lithospheric thickness, L, as a scale length and using a scale velocity, U_0, whence

$$\dot{\varepsilon}'_{ij} = \dot{\varepsilon}_{ij}\frac{L}{U_0} \tag{A18}$$

$$\overline{\tau}'_{ij} = \frac{\overline{\tau}_{ij}}{g\rho_c L(1-\rho_c/\rho_m)} = \frac{\dot{\varepsilon}'_{ij}\left(\dot{\varepsilon}'_{kl}\dot{\varepsilon}'_{kl}\right)^{1/n-1}}{Ar} \tag{A19}$$

$$\Gamma' = \frac{\Gamma}{g\rho_c L^2(1-\rho_c/\rho_m)} \tag{A20}$$

where Ar is the Argand number [*England and McKenzie*, 1982]

$$Ar = \frac{g\rho_c L(1-\rho_c/\rho_m)}{B\left(U_0/L\right)^{1/n}}, \tag{A21}$$

and all variables are identified in Table 1.

The equations (A14), in their discretized nondimensional form, are solved for u_θ, u_ϕ subject to a prescribed set of velocities and forces on the external boundary to the sheet, using a finite element method that was adapted from the method of *Houseman and England* [1986] and *Houseman et al.* [2008] by projecting the spherical problem onto the Cartesian plane using the sinusoidal equal area projection and neglecting the small variation in r. A finite element mesh of approximately equidimensional triangles is generated using the `triangle` program of *Shewchuck* [2002], with the size of the elements being reduced until well-resolved solutions are obtained. This mesh includes nodes at the locations of all GPS measurements used to constrain the calculations (section 2).

With this nondimensionalization, model velocities scale as Ar^n. Because U_0, the scale factor that relates model velocities to observed velocities, is unknown a priori, we choose an arbitrary value of Ar (that results in dimensionless velocities of order 1) and then determine the scale factor U_0 using equation (8). B is then obtained from equation (9). Because U_0 scales as Ar^{-n}, the resulting value of B is independent of our choice of Ar. The Argand number is, therefore, indeterminate in these calculations. This indeterminacy arises because the boundary conditions contain no velocity scale (section 3.2). Had we chosen to specify a nonzero velocity on any part of our solution domain, that choice would have set a velocity scale—hence B—and the Argand number would have become an additional parameter.

Acknowledgments
Lynn Evans has made numerous contributions to the development and maintenance of the 2-D finite element code *basil* used to make the calculations in this paper. We are grateful to many colleagues with whom we have collaborated during three decades of GPS work in this region. Principal among these are B. Aktuğ, A. Avallone, H. Billiris, P. Briole, A. Cingöz, P. Clarke, R. Davies, M. Floyd, A. Kılıçoğlu, A. Kurt, O. Lenk, K. Palamartchouk, D. Paradissis, B. Parsons, C. Raptakis, and G. Veis. This work has been supported by the Natural Environment Research Council through grant NER/A/S/2001/01607, by funding of the National Centre for Earth Observation (COMET+), and by the National Environmental Research Council and the Economic and Social Research Council through grant NE/J02001X/1. The figures were made using GMT [*Wessel and Smith*, 2013]. The data used in this analysis can be found in the supporting information. We thank Z-K Shen for providing the code used for calculating strain rates from GPS measurements. We are grateful to Peter Molnar and an anonymous reviewer for helpful reviews.

References

Aksu, A., J. Hall, and C. Yaltirak (2009), Miocene-recent evolution of Anaximander Mountains and Finike Basin at the junction of Hellenic and Cyprus Arcs, eastern Mediterranean, *Mar. Geol.*, *258*, 24–47.
Aktuğ, B., et al. (2009), Deformation of western Turkey from a combination of permanent and campaign GPS data: Limits to block-like behavior, *J. Geophys. Res.*, *114*, B10404, doi:10.1029/2008JB006000.
Aktuğ, B., E. Parmaksız, M. Kurt, O. Lenk, A. Kılıçoğlu, M. A. Gürdal, and S. Özdemir (2013), Deformation of Central Anatolia: GPS implications, *J. Geodyn.*, *67*, 78–96, doi:10.1016/j.jog.2012.05.008.
Aktuğ, B., A. Doğru, H. Özener, and M. Peyret (2015), Slip rates and locking depth variation along central and easternmost segments of North Anatolian Fault, *Geophys. J. Int.*, *202*(3), 2133–2149.
Armijo, R., B. Meyer, G. King, A. Rigo, and D. Papanastassiou (1996), Quaternary evolution of the Corinth rift and its implications for the late Cenozoic evolution of the Aegean, *Geophys. J. Int.*, *126*(1), 11–53.
Armijo, R., B. Meyer, A. Hubert, and A. Barka (1999), Westward propagation of the North Anatolian fault into the northern Aegean: Timing and kinematics, *Geology*, *27*(3), 267–270.
Armijo, R., F. Flerit, G. King, and B. Meyer (2003), Linear elastic fracture mechanics explains the past and present evolution of the Aegean, *Earth Planet. Sci. Lett.*, *217*, 85–95.
Balmino, G., N. Vales, S. Bonvalot, and A. Briais (2012), Spherical harmonic modelling to ultra-high degree of Bouguer and isostatic anomalies, *J. Geod.*, *86*, 499–520, doi:10.1007/s00190-011-0533-4.
Billiris, H., et al. (1991), Geodetic determination of tectonic deformation in central Greece from 1900 to 1988, *Nature*, *350*, 124–129.
Bird, P., and K. Piper (1980), Plane-stress finite-element models of tectonic flow in Southern California, *Phys. Earth Planet. Inter.*, *21*, 158–175.
Bourne, S., P. England, and B. Parsons (1998), The motion of crustal blocks driven by flow of the lower lithosphere and implications for slip rates of continental strike-slip faults, *Nature*, *391*, 655–659.
Burchfiel, B., R. King, A. Todosov, V. Kotzev, N. Durmurdzanov, T. Serafimovski, and B. Nurce (2006), GPS results for Macedonia and its importance for the tectonics of the southern Balkan extensional regime, *Tectonophysics*, *413*(3–4), 239–248.

Cianetti, S., P. Gasperini, C. Giunchi, and E. Boschi (2001), Numerical modelling of the Aegean–Anatolian region: Geodynamical constraints from observed rheological heterogeneities, *Geophys. J. Int.*, *146*(3), 760–780.
Clarke, P. J., et al. (1998), Crustal strain in central Greece from repeated GPS measurements in the interval 1989–1997, *Geophys. J. Int.*, *135*(1), 195–214.
D'Agostino, N., A. Avallone, D. Cheloni, E. D'Anastasio, S. Mantenuto, and G. Selvaggi (2008), Active tectonics of the Adriatic region from GPS and earthquake slip vectors, *J. Geophys. Res.*, *113*, B12413, doi:10.1029/2008JB005860.
Davies, R., P. England, B. Parsons, H. Billiris, D. Paradissis, and G. Veis (1997), Geodetic strain of Greece in the interval 1892–1992, *J. Geophys. Res.*, *102*(B11), 24,571–24,588.
Dyson, F. (2004), A meeting with Enrico Fermi, *Nature*, *427*(6972), 297–297.
Dziewonski, A. M., T.-A. Chou, and J. H. Woodhouse (1981), Determination of earthquake source parameters from waveform data for studies of global and regional seismicity, *J. Geophys. Res.*, *86*, 2825–2852.
Ekström, G., M. Nettles, and A. Dziewonski (2012), The Global CMT Project 2004–2010: Centroid-moment tensors for 13,017 earthquakes, *Phys. Earth Planet. Inter.*, *200-201*, 1–9.
England, P., and D. McKenzie (1982), A thin viscous sheet model for continental deformation, *Geophys. J. R. Astron. Soc.*, *70*, 295–321.
England, P., and D. McKenzie (1983), Correction to a thin viscous sheet model for continental deformation, *Geophys. J. R. Astron. Soc.*, *73*, 523–532.
England, P., G. Houseman, and L. Sonder (1985), Length scales for continental deformation in convergent, divergent and strike-slip environments: Analytical and approximate solutions for a thin viscous sheet model, *J. Geophys. Res.*, *90*, 3551–3557.
Faccenna, C., et al. (2014), Mantle dynamics in the Mediterranean, *Rev. Geophys.*, *52*, 283–332, doi:10.1002/2013RG000444.
Fischer, K. (2006), The influence of different rheological parameters on the surface deformation and stress field of the Aegean–Anatolian region, *Int. J. Earth Sci.*, *95*(2), 239–249, (Geol Rundsch).
Flerit, F., R. Armijo, G. King, and B. Meyer (2004), The mechanical interaction between the propagating North Anatolian Fault and the back-arc extension in the Aegean, *Earth Planet. Sci. Lett.*, *224*(3–4), 347–362.
Floyd, M. A., H. Billiris, D. Paradissis, G. Veis, A. Avallone, P. Briole, S. McClusky, J.-M. Nocquet, B. Parsons, and P. C. England (2010), A new velocity field for Greece: Implications for the kinematics and dynamics of the Aegean, *J. Geophys. Res.*, *115*, B10403, doi:10.1029/2009JB007040.
Ganas, A., and T. Parsons (2009), Three-dimensional model of Hellenic Arc deformation and origin of the Cretan uplift, *J. Geophys. Res.*, *114*, B06404, doi:10.1029/2008JB005599.
Garthwaite, M. C., and G. A. Houseman (2011), Validity of the thin viscous sheet approximation in models of continental collision, *J. Geophys. Res.*, *116*, B02404, doi:10.1029/2010JB007770.
Goldsworthy, M., and J. Jackson (2001), Migration of activity within normal fault systems: Examples from the Quaternary of mainland Greece, *J. Struct. Geol.*, *23*(2–3), 489–506.
Goldsworthy, M., and J. A. Jackson (2000), Active normal fault evolution and interaction in Greece revealed by geomorphology and drainange patterns, *J. Geol. Soc. London*, *157*, 967–981.
Goldsworthy, M., J. Jackson, and J. Haines (2002), The continuity of active fault systems in Greece, *Geophys. J. Int.*, *148*(3), 596–618.
Gordon, R. G., and G. A. Houseman (2015), Deformation of Indian Ocean lithosphere: Evidence for a highly nonlinear rheological law, *J. Geophys. Res. Solid Earth*, *120*, 4434–4449, doi:10.1002/2015JB011993.
Hall, J., A. E. Aksu, C. Yaltirak, and J. D. Winsor (2009), Structural architecture of the Rhodes Basin: A deep depocentre that evolved since the Pliocene at the junction of Hellenic and Cyprus Arcs, eastern Mediterranean, *Mar. Geol.*, *258*(1–4), 1–23, doi:10.1016/j.margeo.2008.02.007.
Hammond, W. C., G. Blewitt, and C. Kreemer (2011), Block modeling of crustal deformation of the northern Walker Lane and Basin and Range from GPS velocities, *J. Geophys. Res.*, *116*, B04402, doi:10.1029/2010JB007817.
Hatzfeld, D., J. Martinod, G. Bastet, and P. Gautier (1997), An analog experiment for the Aegean to describe the contribution of gravitational potential energy, *J. Geophys. Res.*, *102*(B1), 649–660.
Haxby, W. F., and D. L. Turcotte (1978), On isostatic geoid anomalies, *J. Geophys. Res.*, *83*(B11), 5473–5478.
Hollenstein, C., M. D. Müller, A. Geiger, and H.-G. Kahle (2008), Crustal motion and deformation in Greece from a decade of GPS measurements, 1993–2003, *Tectonophysics*, *449*(1–4), 17–40.
Houseman, G., and P. England (1986), Finite strain calculations of continental deformation 1. Method and general results for convergent zones, *J. Geophys. Res.*, *91*(B3), 3651–3663.
Houseman, G., T. Barr, and L. Evans (2008), Basil: Stress and deformation in a viscous material, in *Microdynamics Simulation, Lect. Notes Earth Sci.*, vol. 106, edited by P. D. Bons, D. Koehn, and M. W. Jessell, pp. 77–85, Springer, Berlin.
International Seismological Centre (2011), *EHB Bulletin*, Int. Seis. Cent., Thatcham, U. K. [Available at http://www.isc.ac.uk.]
Jackson, J. (1994), Active tectonics of the Aegean region, *Annu. Rev. Earth Planet. Sci.*, *22*, 239–271.
Jackson, J., and D. P. McKenzie (1988), The relationship between plate motions and seismic moment tensors and the rate of active deformation in the Mediterranean and Middle East, *Geophys. J. R. Astron. Soc.*, *93*, 45–73.
Kotzev, V., R. Nakov, T. Georgiev, B. Burchfiel, and R. King (2006), Crustal motion and strain accumulation in western Bulgaria, *Tectonophysics*, *413*(3–4), 127–145.
Le Pichon, X. (1982), Land-locked oceanic basins and continental collision: The Eastern Mediterranean as a case example, in *Mountain Building Processes*, edited by K. Hsü, pp. 129–146, Academic Press, London.
Le Pichon, X., and J. Angelier (1979), The Hellenic Trench system: A key to the neotectonic evolution of the Eastern Mediterranean area, *Tectonophysics*, *60*, 1–42.
Le Pichon, X., and C. Kreemer (2010), The Miocene-to-present kinematic evolution of the Eastern Mediterranean and Middle East and its implications for dynamics, *Annu. Rev. Earth Planet. Sci.*, *38*(1), 323–351.
Le Pichon, X., N. Chamot-Rooke, S. Lallemant, R. Noomen, and G. Veis (1995), Geodetic determination of the kinematics of central Greece with respect to Europe: Implications for eastern Mediterranean tectonics, *J. Geophys. Res.*, *100*(B7), 12,675–12,690.
Martinod, J., D. Hatzfeld, J. Brun, P. Davy, and P. Gautier (2000), Continental collision, gravity spreading, and kinematics of Aegea and Anatolia, *Tectonics*, *19*(2), 290–299.
Mascle, J., and E. Chaumillon (1998), An overview of Mediterranean Ridge collisional accretionary complex as deduced from multichannel seismic data, *Geo-Mar. Lett.*, *18*, 81–89.
McClusky, S., et al. (2000), Global Positioning System constraints on plate kinematics and dynamics in the eastern Mediterranean and Caucasus, *J. Geophys. Res.*, *105*(B3), 5695–5719.
McKenzie, D. (1972), Active tectonics of the Mediterranean region, *Geophys. J. R. Astron. Soc.*, *30*(2), 109–185.

McKenzie, D. (1978), Active tectonics of the Alpine-Himalayan belt—Aegean Sea and surrounding regions, *Geophys. J. R. Astron. Soc.*, *55*, 217–254.
Meade, B. J., and B. H. Hager (2005), Block models of crustal motion in Southern California constrained by GPS measurements, *J. Geophys. Res.*, *110*, B03403, doi:10.1029/2004JB003209.
Meade, B. J., B. H. Hager, S. C. McClusky, R. E. Reilinger, S. Ergintav, O. Lenk, A. Barka, and H. Özener (2002), Estimates of seismic potential in the Marmara Sea region from block models of secular deformation constrained by Global Positioning System measurements, *Bull. Seismol. Soc. Am.*, *92*(1), 208–215.
Métois, M., N. D'Agostino, A. Avallone, N. Chamot-Rooke, A. Rabaute, L. Duni, N. Kuka, R. Koci, and I. Georgiev (2015), Insights on continental collisional processes from GPS data: Dynamics of the Peri-Adriatic belts, *J. Geophys. Res. Solid Earth*, *120*, 8701–8719, doi:10.1002/2015JB012023.
Molnar, P., and T. Atwater (1978), Interarc spreading and Cordilleran tectonics as alternates related to the age of subducted oceanic lithosphere, *Earth Planet. Sci. Lett.*, *41*(3), 330–340.
Molnar, P., and P. Tapponnier (1978), Active tectonics of Tibet, *J. Geophys. Res.*, *83*, 2648–2682.
Molnar, P., P. C. England, and C. H. Jones (2015), Mantle dynamics, isostasy, and the support of high terrain, *J. Geophys. Res. Solid Earth*, *120*, 1932–1957, doi:10.1002/2014JB011724.
Nanjo, K. Z., and D. L. Turcotte (2005), Damage and rheology in a fibre-bundle model, *Geophys. J. Int.*, *162*(3), 859–866.
Nocquet, J.-M. (2012), Present-day kinematics of the Mediterranean: A comprehensive overview of GPS results, *Tectonophysics*, *579*, 220–242, doi:10.1016/j.tecto.2012.03.037.
Nyst, M., and W. Thatcher (2004), New constraints on the active tectonic deformation of the Aegean, *J. Geophys. Res.*, *109*, B11406, doi:10.1029/2003JB002830.
Ozener, H., E. Arpat, S. Ergintav, A. Dogru, R. Cakmak, B. Turgut, and U. Dogan (2010), Kinematics of the eastern part of the North Anatolian fault zone, *J. Geodyn.*, *49*(3), 141–150.
Özeren, M., and W. Holt (2010), The dynamics of the eastern Mediterranean and eastern Turkey, *Geophys. J. Int.*, *183*(3), 1165–1184.
Pérouse, E., N. Chamot-Rooke, A. Rabaute, P. Briole, F. Jouanne, I. Georgiev, and D. Dimitrov (2012), Bridging onshore and offshore present-day kinematics of central and eastern Mediterranean: Implications for crustal dynamics and mantle flow, *Geochem. Geophys. Geosyst.*, *13*, Q09013, doi:10.1029/2012GC004289.
Reilinger, R., et al. (2006), GPS constraints on continental deformation in the Africa-Arabia-Eurasia continental collision zone and implications for the dynamics of plate interactions, *J. Geophys. Res.*, *111*, B05411, doi:10.1029/2005JB004051.
Reilinger, R., S. McClusky, D. Paradissis, S. Ergintav, and P. Vernant (2009), Geodetic constraints on the tectonic evolution of the Aegean region and strain accumulation along the Hellenic subduction zone, *Tectonophysics*, *488*, 22–30.
Royden, L. (1993), The tectonic expression of slab pull at continental convergent boundaries, *Tectonics*, *12*, 303–325.
Şaroglu, F., Ö. Emre, and İ. Kuşçu (1992), *Active Fault Map of Turkey*, General Directorate of Mineral Research and Exploration (MTA), Eskişehir Yolu, Ankara, Turkey.
Schmalholz, S. M., S. Medvedev, S. M. Lechmann, and Y. Podladchikov (2014), Relationship between tectonic overpressure, deviatoric stress, driving force, isostasy and gravitational potential energy, *Geophys. J. Int.*, *197*(2), 680–696, doi:10.1093/gji/ggu040.
Şengör, A. M. Ç., N. Görür, and F. Şaroğlu (1985), Strike slip faulting and related basin formation in zones of tectonic escape: Turkey as a case study, in *Strike Slip Deformation, Basin Formation, and Sedimentation*, vol. 37, edited by K. T. Biddle and N. Christie-Blick, pp. 227–264, Soc. of Econ. Paleontol. and Mineral., Tulsa, Okla.
Shaw, B., and J. Jackson (2010), Earthquake mechanisms and active tectonics of the Hellenic subduction zone, *Geophys. J. Int.*, *181*, 966–984.
Shen, Z.-K., M. Wang, Y. Zeng, and F. Wang (2015), Optimal interpolation of spatially discretized geodetic data, *Bull. Seismol. Soc. Am.*, *105*(4), 2117–2127.
Shewchuck, J. R. (2002), Delaunay refinement algorithms for triangular mesh generation, *Comput. Geom. Theory Appl.*, *22*, 21–74.
Sonder, L., and P. England (1986), Vertical averages of rheology of the continental lithosphere: Relation to thin sheet parameters, *Earth Planet. Sci. Lett.*, *77*(1), 81–90.
Sonder, L., P. England, and G. Houseman (1986), Continuum calculations of continental deformation in transcurrent environments, *J. Geophys. Res.*, *91*, 4797–4810.
Tatar, O., et al. (2012), Crustal deformation and kinematics of the eastern part of the North Anatolian Fault zone (Turkey) from GPS measurements, *Tectonophysics*, *518–521*, 55–62, doi:10.1016/j.tecto.2011.11.010.
Taymaz, T., J. Jackson, and D. McKenzie (1991a), Active tectonics of the north and central Aegean Sea, *Geophys. J. Int.*, *106*(2), 433–490.
Taymaz, T., H. Eyidoğan, and J. Jackson (1991b), Source parameters of large earthquakes in the East Anatolian fault zone (Turkey), *Geophys. J. Int.*, *106*, 537–550.
ten Veen, J., J. Woodside, T. Zitter, J. Dumont, J. Mascle, and A. Volkonskaia (2004), Neotectonic evolution of the Anaximander Mountains at the junction of the Hellenic and Cyprus arcs, *Tectonophysics*, *391*(1–4), 35–65.
Turcotte, D. L., and G. Schubert (2014), *Geodynamics*, 3rd ed., Cambridge Univ. Press, Cambridge, U. K.
Vernant, P., R. Reilinger, and S. McClusky (2014), Geodetic evidence for low coupling on the Hellenic subduction plate interface, *Earth Planet. Sci. Lett.*, *385*, 122–129, doi:10.1016/j.epsl.2013.10.018.
Wallace, L. M., J. Beavan, R. McCaffrey, K. Berryman, and P. Denys (2007), Balancing the plate motion budget in the South Island, New Zealand using GPS, geological and seismological data, *Geophys. J. Int.*, *168*(1), 332–352.
Wessel, P., and W. H. F. Smith (2013), Generic mapping tools: Improved version released, *Eos Trans. AGU*, *94*, 409–410.
Woodside, J., J. Mascle, T. Zitter, A. Limonov, M. Ergun, and A. Volkonskaia (2002), The Florence Rise, the western bend of the Cyprus Arc, *Mar. Geol.*, *185*(3–4), 177–194.
Yavaşoğlu, H., O. Tarı, E. Tüysüz, Z. Çakir, and S. Ergintav (2010), Determining and modeling tectonic movements along the central part of the North Anatolian Fault (Turkey) using geodetic measurements, *J. Geodyn.*, *51*, 339–343.